

Highlights

A Generalised Maxwell Stress Tensor for Semi-Analytic Force and Torque Between Permanent Magnets, Coils, and Soft Iron

Matthew Forbes, William S. P. Robertson, Anthony C. Zander, James Vidler, Johannes J. H. Paulides

- Electromagnetic stress tensor that is a function of two arbitrary vector fields
- Improved numerical accuracy of force density with discretisation of analytic fields
- Semi-analytic application in 2D/3D linear or nonlinear actuator models
- Validation with comparison to exact analytic solutions and/or finite element models
- The tensor can be extended to multiphysics applications

A Generalised Maxwell Stress Tensor for Semi-Analytic Force and Torque Between Permanent Magnets, Coils, and Soft Iron

Matthew Forbes^{a,*}, William S. P. Robertson^a, Anthony C. Zander^a, James Vidler^a, Johannes J. H. Paulides^b

^a*The University of Adelaide, North Terrace, Adelaide, 5005, SA, Australia*

^b*Advanced Electromagnetics Group, Industrieweg 78, Waalwijk, 5145 PW, The Netherlands*

Abstract

The Maxwell Stress Tensor is a computationally efficient method for calculating the force and torque between two arbitrary collections of rigidly-connected permanent magnets, coils, and/or iron (soft magnet) segments, when using exact analytic magnetic field solutions. However, use of the tensor exacerbates numerical errors present in the closed-surface free space mesh of a region, whether that be from an approximate field solution such as a finite sum, or discretisation errors that create a numeric non-zero divergence. Using a specialised identity of the divergence theorem, this article derives a generalised Maxwell Stress Tensor, which is interchangeable with the standard form and significantly reduces or removes numerical error sources from the meshing. The application focus of this work is modelling of non-periodic permanent magnet machines without geometrical assumptions through superposition of analytic magnetic field solutions (B and H) from a large number of elements. The influence of relative permeability can be included in these elements through varying the volumetric magnetic charge or current densities. Case studies with analytic or finite element force solutions are used to verify the result and compare the accuracy and computational efficiency with traditional semi-analytic methods. The proposed tensor enables parametric studies with accuracy not previously possible using an elemental modelling method, and can be applied to existing multiphysics models.

Keywords: Magnetic field modelling, Exact analytical solution, Magnetostatics, Divergence theorem identity, Linear synchronous motor

*Corresponding author
Email address: matthew.forbes@adelaide.edu.au (Matthew Forbes)

1. Introduction

Various arrangements of permanent magnets (PMs), coils, and soft iron segments are found in modern devices, with Finite Element Analysis (FEA) being the predominant tool in industry for the modelling and design. While FEA is the industry standard, it is a computationally expensive method for large parametric studies, and the results should be verified using an alternate method if one exists. In the literature and academia, there are a vast number of alternate analytic, numeric, and hybrid methods developed to optimise the trade-off between computation time and accuracy, compared and validated to FEA [1, 2, 3, 4, 5]. The benefit of using analytic magnetic field solutions is they are valid in an unbounded region, and due to superposition, an entire model does not need to be rerun for basic design changes, e.g. changing the size, location, geometry, strength, of a single PM without loss of generality. Regions with nonlinearities in an analytic model can be represented with local discretisation (or linearisation) [6, 7], that unlike FEA, can preserve curved surfaces. As we are using a complete description of the field, it is possible to extend the model to dynamic effects such as eddy-currents in the iron and magnets, hysteresis, or back EMF in the coils [8]. A required step toward a general magnetic framework is numerically stable and accurate semi-analytic force and torque calculations, with competing analytical methods being multipole expansions and elemental solutions.

The traditional analytical modelling method for periodic PM machines is to describe the field using a multipole expansion [9, 10, 11], a lumped source function that allows force and torque calculation by (typically) assuming that iron has infinite permeability, interfaces between boundaries are plane, and constant magnet properties between boundary layers. Elemental magnetic field solutions model each permanent magnet or coil source individually, removing common assumptions on geometry, topology, permeability, and periodicity, that are present in models using a multiple expansion. However, an elemental model has significant complexities for accurate force and torque calculation, as will be discussed in this article. The method presented in this article is general and can be used for arbitrary arrangements of magnets as shown in Figure 1a, and can be used to solve practical problems, such as the actuator design shown in Figure 1b. These nuances allow modelling of unique designs that reduce thermal limitations [12], or assessment of potential vibrations from eccentricity [13].

Analytic magnetic field solutions are of great interest for understanding complex interactions as they can be exact and, *if* computationally efficient, are ideal for use in large parametric studies. However, analytic solutions for the magnetic forces often require a semi-analytic discretisation approach [14]. For instance, Figure 1 shows two collections of magnetic elements of various shapes and sizes. The magnetic field for each individual volume may be derived in the literature, but the analytic equation for the force acting between all permutable pairs may not be known (Figure 1a entails 9 unique interactions between each element). Analytic force solutions for each pair of geometries in the general case are not practically feasible to find, unless one particular permutation is relevant for a specific application — analytic solutions in this case heavily rely upon degenerate cases, such as specific geometric ratios and/or alignments between regions [15]. Even if we did know all the analytic force solutions, there is a problem of scaling: if we increased the number of magnetic sources in both collections of Figure 1, then the number of computations will scale quadratically. Therefore, we require general methods for finding the force and torque between any permutable combination of macroscopic magnetic objects, on the proviso that the field from each is known exactly. Using the magnetic charge, current, and filament models (Section 2), the distance between all source and field points is exactly described, allowing accurate torque descriptions.

In the absence of a closed-form analytic force solution, a boundary integral method using the classical Maxwell Stress Tensor (MST) is arguably the most general computational method, as a single closed surface can be formed around any number of unique,

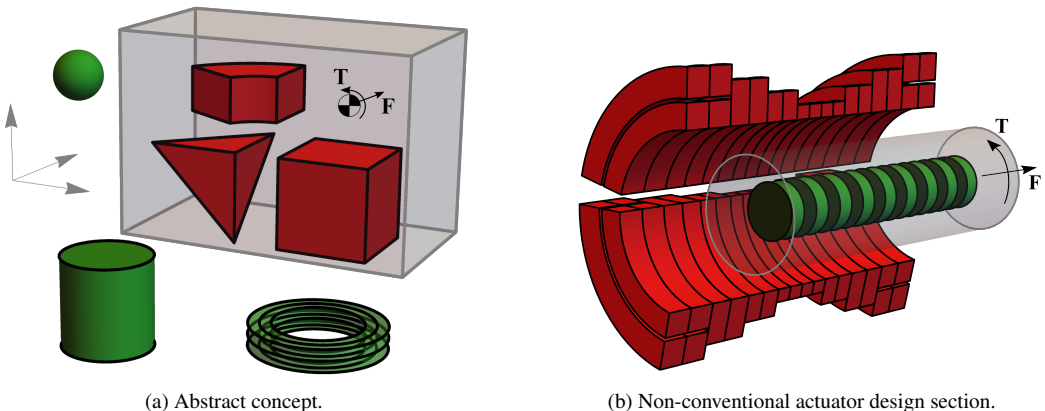


Figure 1: Two example magnetic systems, each containing two collections (one red, one green) of rigidly-connected homogeneous magnetic field sources, of arbitrary location and geometry. This is defined as an elemental magnetic model, whereby each magnetic source is uniquely defined. The global magnetostatic force and torque (\mathbf{F}, \mathbf{T}) interactions can be found through a region (shaded in grey) on the source locations with superposition, or generalised over a bounding region surface using the divergence theorem.

mesh-free, source elements (as illustrated in Figure 1). The MST is an analytic method if the stray field across the surface is a known function, although this is only practical with approximation or with simple fields. Due to the complexity of an exact magnetic field in an elemental model, the MST is realised as a semi-analytic method that requires the introduction of a meshed region; however, for each mesh element, the number of field calculations scales linearly with the addition of magnetic sources as opposed to quadratically with the number of direct force calculations. Due to the MST mesh introducing error (or inaccuracy) from a non-zero divergence or within the curl, it is *numerically* possible to yield results with highly non-physical interpretations, including: forces on a region containing a complete absence of matter; or, a sum of torques that does not maintain a balance of angular momentum. These errors are inherently present if the analytic field solution is represented as an exact infinite series, for which a finite sum must be computed for many model elements, introducing truncation error. Errors are predominantly reported when using numeric computation methods such as FEA [16], LBM [17], or NOM [18], but not when using elemental semi-analytic solutions [19].

It is recalled that the MST is simply derived from the macroscopic Lorentz force, using a vector identity and application of the divergence theorem. The classical MST form is a function with an input of all field sources superimposed, yet this can be an arbitrary choice of any number of vector fields. To rectify numerical issues with the MST, the authors propose a generalised Maxwell Stress Tensor (GMST) form which is directly interchangeable with the MST.

The scope of this article is limited to global effects, whereby the predominant force models discussed in literature (Lorentz, Einstein-Laub, Minkowski, Abraham, Chu) can all be shown to produce the correct global force, but one may be more appropriate in different applications or experiments [20]. Dependent on local effects, the cited force models can disagree when extended to torques [21], although the MST is consistent with the Lorentz force, given a symmetric tensor [22, §3.9]. Extension of the MST to include local effects, such as the deformation of materials, cannot be done without additional mechanical coupling terms as that would imply the deformation is completely described by a change in the field distribution [23, 24]. The MST can be combined with continuum mechanics to consider local force and strain distributions with magnetostriction or ferrofluids [25, 23, 26]. Another multiphysics application is in electromagnetic noise models, where the time-space field variance leads to structural vibration and acoustic radiation in electric motors [27]. This article only considers rigid structures where the two collections of elements are not in contact, though the proposed GMST may be applied to literature that uses the MST in these cases [28, 29]. The analytic force solutions and semi-analytic MST/GMST models in this article are undefined when the two collections are in contact: there is an overlap of two surfaces of discontinuity in the external magnetic field and magnetic body (internal to the bounding surface, any element can overlap or be in contact). Alternatively, an inelegant yet effective ‘virtual air gap’ [30] can be applied in this limiting case, separating the bodies by machine precision (‘epsilon’) to ensure the MST surface does not cross a magnetic field discontinuity. The work contained herein pertains only to the magnetic field; however, the identities presented can be readily applied to the symmetric electric field components. A summary of results and potential applications from this article is:

- The GMST is derived using a divergence theorem identity, that to the best of the authors’ knowledge, has not been applied in electromagnetic modelling before;
- Compared to the MST, the GMST is beneficial for reducing numerical error and improving convergence time in force and torque results using discretised exact analytic magnetic field distributions;
- Across several case studies, results are demonstrated between cylindrical geometries that have complex magnetic field solutions. The GMST is general and can be extended to any geometry/source with known field solutions, e.g. complex geometries with plane boundaries have closed-form magnetic field solutions using superposition of polyhedra [31];
- The GMST is a computationally efficient analytic based method for use within complex 3D models for calculating force and torque. The GMST force density can be used within numeric multiphysics models, such as electromagnetic noise in structures or the motion of ferrofluids.

In this article, Section 2 reviews the connection between the Lorentz and Maxwell (MST) force equations, in the context of the charge, current, and filament magnetic field models. The computational efficiency of each force equation is assessed, and an alternate divergence theorem identity is introduced. Section 3 derives alternate tensors for the force and torque (GMST), for which the MST is a special case. Section 4 introduces the computational methods to use analytic magnetic field solutions in semi-analytic force equations. Six engineering case studies are shown that use the elemental model to compare force and torque calculated with the MST, GMST, and FEA, to analytic solutions in Section 5 and numeric solutions in Section 6.

2. Background and problem formulation

In this section the magnetic charge, current, and filament models are introduced as traditional force computation methods for an elemental model, whereby the field is evaluated at source locations. These models are then related to the MST, where the field is calculated away from source locations, and the semi-analytic computational efficiencies are assessed relative to an analytic force model.

Analytic formulations of the magnetostatic field can be found for regions of uniform magnetisation or current, within homogeneous media with constant properties. Examples include cuboid magnets [32], polyhedron magnets [31], and cylindrical magnets and coils [33]. Time variance is removed from Maxwell's equations in analytic formulations as it is assumed that at a point in time, the global effects from all sources of magnetic fields have reached steady state. Nonlinear matter, such as iron or permanent magnets with a non-unity permeability, can be approximated by discretisation with an equivalent set of linear permanent magnets using an iterative process [34] (Appendix A).

The magnetisation has mathematically equal magnetic field solutions due to either a bound, equivalent current distribution (current model, $\mathbf{M}_J \text{ A}\cdot\text{m}^{-1}$) or equivalent charge distribution (charge model, $\mathbf{M}_\varrho \text{ A}\cdot\text{m}^{-1}$). The current distribution must also be bound, so that through a cross section, it can be resolved into current loops that close upon themselves (filament model, $\mathbf{J} \text{ A}\cdot\text{m}^{-2}$). The current and charge models are useful for modelling permanent magnets that have a relative permeability close to unity, and the filament model is useful for modelling stranded coils with static, direct current.

2.1. The Lorentz and Maxwell force models

The macroscopic generalised Lorentz volume force density \mathbf{f} acting on the collection of rigid sources (static current and bound current or 'magnetic charge' from remanence) is [33, §A.4]

$$\mathbf{f} = \mathbf{J} \times \mathbf{B}_E + \mathbf{M}_J \cdot (\nabla \mathbf{B}_E) + (\nabla \mathbf{B}_E) \cdot \mathbf{M}_\varrho, \quad (1)$$

where $\mathbf{B}_E (\text{N}\cdot\text{A}^{-1}\cdot\text{m}^{-1})$ is the magnetic field superposition from all external sources. This excludes the self-fields from \mathbf{J} , \mathbf{M}_J , and \mathbf{M}_ϱ as there are no self-forces. From (1), the total Lorentz force \mathbf{F} includes surface and filament currents ($\mathbf{K} \text{ A}\cdot\text{m}^{-1}$, $\mathbf{I} \text{ A}$) along with boundary conditions for the magnetised regions [35, §3]

$$\mathbf{F}_L = \sum_i \mathbf{F}_{\text{Filament}}^{(i)} + \sum_j \mathbf{F}_{\text{Current}}^{(j)} + \sum_k \mathbf{F}_{\text{Charge}}^{(k)} \quad (2)$$

$$\begin{aligned} \mathbf{F}_{\text{Filament}}^{(i)} &= \int_{V^{(i)}} \mathbf{J}^{(i)} \times \mathbf{B}_E \, dv + \int_{S^{(i)}} \mathbf{K}^{(i)} \times \mathbf{B}_E \, da + \int_{C^{(i)}} \mathbf{I}^{(i)} \times \mathbf{B}_E \, dl \\ \mathbf{F}_{\text{Current}}^{(j)} &= \int_{V^{(j)}} (\nabla \times \mathbf{M}_J^{(j)}) \times \mathbf{B}_E \, dv + \oint_{S^{(j)}} (\mathbf{M}_J^{(j)} \times \mathbf{n}) \times \mathbf{B}_E \, ds \\ \mathbf{F}_{\text{Charge}}^{(k)} &= \oint_{S^{(k)}} (\mathbf{M}_\varrho^{(k)} \cdot \mathbf{n}) \mathbf{B}_E \, ds - \int_{V^{(k)}} (\nabla \cdot \mathbf{M}_\varrho^{(k)}) \mathbf{B}_E \, dv, \end{aligned} \quad (3)$$

where there are i regions with $\mathbf{J}^{(i)}$, j regions with $\mathbf{M}_J^{(j)}$, and k regions with $\mathbf{M}_\varrho^{(k)}$. The purpose of showing equation (2) is to highlight complexity in meshing the various integration regions (in lieu of a suitable analytic solution), especially when these change dependent upon whether a magnetised region is modelled with the charge or current model.

To abstract the mesh away from the location of the sources, the magnetic field can be defined as a force density: given two magnetic field components, the product $\mu_0^{-1} B_1 B_2$ gives a surface force density $\text{N}\cdot\text{m}^{-2}$, where $\mu_0 (\text{N}\cdot\text{A}^{-2})$ is the permeability of free space. Consequently, if \mathbf{J} is a generalised vector current that describes all sources (direct current and/or equivalent remanent magnetisation), then we can rewrite the macroscopic Lorentz force density (1) and apply Ampère's law to give

$$\mathbf{f} \equiv \mathbf{J} \times \mathbf{B} = \mu_0^{-1} (\nabla \times \mathbf{B}) \times \mathbf{B}. \quad (4)$$

The force is

$$\mathbf{F} = \int_V \mathbf{f} \, dv = \mu_0^{-1} \int_V (\nabla \times \mathbf{B}) \times \mathbf{B} \, dv, \quad (5)$$

with a volume integral that can be transformed into a surface integral by introducing the MST, tensor-dyadic \mathcal{M}

$$\begin{aligned} \mathcal{M}(\mathbf{B}) &= \mu_0^{-1} [\mathbf{B} \otimes \mathbf{B} - \frac{1}{2}(\mathbf{B} \cdot \mathbf{B})\mathcal{I}], \\ &= \frac{1}{\mu_0} \begin{bmatrix} B_x^2 - \frac{1}{2}|\mathbf{B}|^2 & B_x B_y & B_x B_z \\ B_y B_x & B_y^2 - \frac{1}{2}|\mathbf{B}|^2 & B_y B_z \\ B_z B_x & B_z B_y & B_z^2 - \frac{1}{2}|\mathbf{B}|^2 \end{bmatrix}, \end{aligned} \quad (6)$$

with tensor product \otimes , idemfactor (or identity tensor) \mathcal{I} , and magnetic field $\mathbf{B} = B_x \mathbf{e}_x + B_y \mathbf{e}_y + B_z \mathbf{e}_z$ that is the superposition from all sources. The MST and proceeding tensors are coordinate invariant. The divergence of this tensor is

$$\nabla \cdot \mathcal{M}(\mathbf{B}) = \mu_0^{-1} [(\nabla \times \mathbf{B}) \times \mathbf{B} + \underbrace{\mathbf{B}(\nabla \cdot \mathbf{B})}] \quad (7)$$

that has the addition of an ‘analytically zero’ term to form the symmetric tensor. Due to Maxwell’s equations, this divergence of \mathbf{B} vanishes, and therefore (5) may be rewritten using the divergence theorem

$$\mathbf{F}_{\text{MST}}(\mathbf{B}) = \int_V \nabla \cdot \mathcal{M}(\mathbf{B}) \, dv = \oint_S \mathcal{M}(\mathbf{B}) \cdot \mathbf{n} \, ds. \quad (8)$$

If it is valid to apply the above divergence theorem, then the total force requires solely a single bounding surface to mesh.

2.2. Computational efficiency

An ideal general force model could be envisaged as being mesh-free, containing only closed-form analytic solutions. This would comprise discrete analytic solutions between all elemental pairs, giving an analytic force solution as the sum of all permutable pairs:

$$\mathbf{F}_A = \sum_n^{m_1 \cdot m_2} \mathbf{F}^{(n)}, \quad (9)$$

where n is the number of force calculations, m_1 and m_2 are two separate groups of rigidly-connected magnetic field sources. From the authors experience, a fair approximation for the computation time of a single force calculation is approximately that of a single magnetic field point $\mathbf{B}^{(n)}$ [33, §6.1]. Analytic magnetic field solutions solve quickly but are mathematically complex, typically involving elliptic integrals or other special functions. As such, the force, which requires integration of the field, is rarely obtainable in closed form. Thus, a meshed solution is unavoidable for a reasonable and efficient computation of the force, requiring semi-analytic boundary element methods to be explored.

Firstly, there are a number of challenges with the Lorentz model (2) when meshing \mathbf{B}_E on the sources $\{\mathbf{J}, \mathbf{M}_J, \mathbf{M}_Q\}$. The number of field calculations (from m_1) scales multiplicatively with the number of meshed sources (m_2), with equal p numbers of field points in each mesh:

$$\mathbf{F}_L \propto \sum_n^{m_1 \cdot m_2 \cdot p} \mathbf{B}_E^{(n)}. \quad (10)$$

Towards optimisation of this calculation, as there are multiple models to describe a remanent magnetisation that produce equivalent magnetic fields, it becomes an ambiguous decision on what the force is acting upon (charges, current) and where \mathbf{B}_E should be calculated (surface, volume).

For the MST, an analytic solution of \mathbf{B} contains an exact description of a field point relative to a source point, thus (8) can be considered to have abstracted the information of \mathbf{J} , removing consideration of mesh location on the sources. This can provide a computational advantage relative to (10) since there is a single surface not multiplicative of the total number of sources $m = m_1 + m_2$

$$\mathbf{F}_{\text{MST}} \propto \sum_n^{p(m_1 + m_2)} \mathbf{B}^{(n)}. \quad (11)$$

If there are an equal number of magnets (or coils) in both groups inside and outside of the surface ($m_1 = m_2$), then (10) scales $O(m^2)$ and (11) scales $O(m)$. This statement has a number of significant caveats, such as assuming equivalent solution convergence for an equal p between both semi-analytic force models, and that the computational time of the internal magnetic field sources is comparable to that of the external sources. The analytic force solution has a similar $O(m^2)$ scaling without the mesh requirement, and will experience a computational burden with a large number of elements.

The disadvantage of using the MST are numerical errors due to the meshing process. Basic assumptions for the field on the MST surface are $\nabla \cdot \mathbf{B} = 0$ and $\nabla \times \mathbf{B} = \mu_0 \mathbf{J}$ — neither hold for a mesh that is coarse relative to the complexity of the field through the bounding surface (non-zero or non-constant valued). This can easily be discovered computing \mathbf{F}_{MST} with $\mathcal{M}(\mathbf{B}_E)$, as will be discussed in Section 3 and demonstrated in Section 5. A solution to reduce or remove such errors is to find a tensor with an additional parameter, one that does not superimpose all sources of \mathbf{B} .

3. The generalised Maxwell stress tensor

In this section, an alternate divergence theorem identity is applied to calculate magnetostatic force and torque, motivated by mesh error sensitivities of the MST. The difference is a definition of two vector fields, that separates magnetic field contributions from sources with a physical interpretation and without loss of generality. It will be shown that this provides both improved convergence compared to the MST (8), and computational efficiency versus the Lorentz model (2) when meshing a large number of magnets and coils. We define the vector field \mathbf{B}_I , that is the sum of all magnetic fields from sources internal to a region \mathcal{V} . We also define the vector field \mathbf{B}_E , that is the sum of all magnetic fields from sources external to a region \mathcal{V} . The surface $\partial\mathcal{V}$ must not intersect a magnetic field source. Whilst we define $\{\mathbf{B}_I, \mathbf{B}_E\}$, the described vector fields are general and could otherwise be labelled $\{\mathbf{B}_1, \mathbf{B}_2\}$

Substitution of $\mathbf{B} = \mathbf{B}_I + \mathbf{B}_E$ into the Lorentz force density (4) and expanding gives

$$\mu_0 \mathbf{f} = (\nabla \times \mathbf{B}_E) \times \mathbf{B}_I + (\nabla \times \mathbf{B}_I) \times \mathbf{B}_E + (\nabla \times \mathbf{B}_E) \times \mathbf{B}_E + (\nabla \times \mathbf{B}_I) \times \mathbf{B}_I. \quad (12)$$

The two groups of magnetic sources corresponding to \mathbf{B}_I and \mathbf{B}_E are rigidly connected, so the last two terms of (12) must vanish. This can otherwise be seen by rewriting (12) in terms of the MST (7)

$$\mu_0 \mathbf{f} = (\nabla \times \mathbf{B}_E) \times \mathbf{B}_I + (\nabla \times \mathbf{B}_I) \times \mathbf{B}_E + \mu_0 \nabla \cdot \mathcal{M}(\mathbf{B}_E) + \mu_0 \nabla \cdot \mathcal{M}(\mathbf{B}_I), \quad (13)$$

where $\mathcal{M}(\mathbf{B}_E)$ implies the absence of ponderable magnetic media in a region and $\mathcal{M}(\mathbf{B}_I)$ implies the absence of ponderable magnetic media outside the region. Thus, the total force is

$$\mu_0 \mathbf{F} = \mu_0 \int_V \mathbf{f} dv = \int_V (\nabla \times \mathbf{B}_E) \times \mathbf{B}_I + (\nabla \times \mathbf{B}_I) \times \mathbf{B}_E dv. \quad (14)$$

3.1. A divergence theorem identity

In a note by Truesdell [36], a generating function is given to derive a number of integral identities equivalent to the divergence theorem. This provides a set of volume integrands that can be written in terms of the divergence of a symmetric tensor, that is important to maintain a balance of linear (force) and angular momentum (torque). We summarise the pertinent results. For arbitrary vector fields \mathbf{b} and \mathbf{c} ,

$$\int_V [(\nabla \times \mathbf{c}) \times \mathbf{b} + (\nabla \times \mathbf{b}) \times \mathbf{c} + \mathbf{b}(\nabla \cdot \mathbf{c}) + \mathbf{c}(\nabla \cdot \mathbf{b})] dv = \oint_S [\mathbf{c} \otimes \mathbf{b} + \mathbf{b} \otimes \mathbf{c} - (\mathbf{c} \cdot \mathbf{b}) \mathcal{I}] \cdot \mathbf{n} ds. \quad (15)$$

A special case of (15) with $\mathbf{b} = \mathbf{c}$ is

$$\int_V [(\nabla \times \mathbf{b}) \times \mathbf{b} + \mathbf{b}(\nabla \cdot \mathbf{b})] dv = \oint_S [\mathbf{b} \otimes \mathbf{b} - \frac{1}{2}(\mathbf{b} \cdot \mathbf{b}) \mathcal{I}] \cdot \mathbf{n} ds. \quad (16)$$

The tensor in the integral on the right is only different by a constant to the MST (6). Introducing a radius vector \mathbf{r} from the coordinate system origin, $\nabla \mathbf{r} = \mathcal{I}$ (and correcting a typographical error in [36]),

$$\int_V [((\nabla \times \mathbf{c}) \times \mathbf{b} + (\nabla \times \mathbf{b}) \times \mathbf{c} + \mathbf{b}(\nabla \cdot \mathbf{c}) + \mathbf{c}(\nabla \cdot \mathbf{b})) \times \mathbf{r}] dv = \oint_S [((\mathbf{c} \otimes \mathbf{b} + \mathbf{b} \otimes \mathbf{c}) \times \mathbf{r}) \cdot \mathbf{n} + ((\mathbf{c} \cdot \mathbf{b}) \mathbf{r}) \times \mathbf{n}] ds. \quad (17)$$

Evaluation of the cross product between a tensor T and vector v uses the notation given (in the Appendix) by Ericksen in [37, pg.795]. In component form, the cross product is $\epsilon_{wrs} T_{pr} v_s$, where ϵ is the Levi-Civita tensor — summed across r, s with indices of w, p . A special case of (17) with $\mathbf{b} = \mathbf{c}$ is the rotation of (16) about \mathbf{r}

$$\int_V \{[(\nabla \times \mathbf{b}) \times \mathbf{b} + \mathbf{b}(\nabla \cdot \mathbf{b})] \times \mathbf{r}\} dv = \oint_S \{[(\mathbf{b} \otimes \mathbf{b}) \times \mathbf{r}] \cdot \mathbf{n} + [\frac{1}{2}(\mathbf{b} \cdot \mathbf{b}) \mathbf{r}] \times \mathbf{n}\} ds. \quad (18)$$

The tensor inside the integral on the right provides the torque corresponding to the MST.

3.2. The force tensor

From the Lorentz force density and splitting the total field into external and internal components (12), we find the relevant magnetostatic divergence theorem identity from (15) with $\mathbf{b} = \mathbf{B}_E$, $\mathbf{c} = \mathbf{B}_I$, and gauges $\nabla \cdot \mathbf{B}_E = 0$ and $\nabla \cdot \mathbf{B}_I = 0$:

$$(\nabla \times \mathbf{B}_E) \times \mathbf{B}_I + (\nabla \times \mathbf{B}_I) \times \mathbf{B}_E + \mathbf{B}_I(\nabla \cdot \mathbf{B}_E) + \mathbf{B}_E(\nabla \cdot \mathbf{B}_I) = \nabla \cdot [\mathbf{B}_E \otimes \mathbf{B}_I + \mathbf{B}_I \otimes \mathbf{B}_E - (\mathbf{B}_E \cdot \mathbf{B}_I) \mathcal{I}] = \mu_0 \nabla \cdot \mathcal{F}(\mathbf{B}_E, \mathbf{B}_I). \quad (19)$$

By analogy with the MST, we define a generalised Maxwell stress tensor (GMST) $\mathcal{F}(\mathbf{B}_E, \mathbf{B}_I)$, that is a function of two vector fields instead of one:

$$\mathbf{F}_{\text{GMST}}(\mathbf{B}_E, \mathbf{B}_I) = \int_V \nabla \cdot \mathcal{F}(\mathbf{B}_E, \mathbf{B}_I) dv = \oint_{\partial V} \mathcal{F}(\mathbf{B}_E, \mathbf{B}_I) \cdot \mathbf{n} ds \quad (20)$$

with $\mathbf{B}_E = B_x^E \mathbf{e}_x + B_y^E \mathbf{e}_y + B_z^E \mathbf{e}_z$ and $\mathbf{B}_I = B_x^I \mathbf{e}_x + B_y^I \mathbf{e}_y + B_z^I \mathbf{e}_z$ and symmetric force tensor

$$\mathcal{F}(\mathbf{B}_E, \mathbf{B}_I) = \frac{1}{\mu_0} \begin{bmatrix} \mathcal{F}_{11} & \mathcal{F}_{12} & \mathcal{F}_{13} \\ \mathcal{F}_{21} & \mathcal{F}_{22} & \mathcal{F}_{23} \\ \mathcal{F}_{31} & \mathcal{F}_{32} & \mathcal{F}_{33} \end{bmatrix},$$

$$\begin{aligned}
\mathcal{F}_{11} &= B_x^E B_x^I - B_y^E B_y^I - B_z^E B_z^I, \\
\mathcal{F}_{22} &= B_y^E B_y^I - B_x^E B_x^I - B_z^E B_z^I, \\
\mathcal{F}_{33} &= B_z^E B_z^I - B_x^E B_x^I - B_y^E B_y^I, \\
\mathcal{F}_{12} = \mathcal{F}_{21} &= B_x^E B_y^I + B_y^E B_x^I, \\
\mathcal{F}_{13} = \mathcal{F}_{31} &= B_x^E B_z^I + B_z^E B_x^I, \\
\mathcal{F}_{23} = \mathcal{F}_{32} &= B_y^E B_z^I + B_z^E B_y^I.
\end{aligned}$$

Intuitively with the GMST, if $\mathbf{B}_E = \mathbf{0}$ or $\mathbf{B}_I = \mathbf{0}$ then there is no force. If we substitute $\mathbf{B} = \mathbf{B}_E + \mathbf{B}_I$ into (8)

$$\mathbf{F}_{\text{MST}}(\mathbf{B}_E + \mathbf{B}_I) = \mathbf{F}_{\text{GMST}}(\mathbf{B}_E, \mathbf{B}_I) + \mathbf{F}_E(\mathbf{B}_E) + \mathbf{F}_I(\mathbf{B}_I), \quad (21)$$

$$\begin{aligned}
\mathbf{F}_E(\mathbf{B}_E) &= \oint_{\partial V} \mathcal{M}(\mathbf{B}_E) \cdot \mathbf{n} \, ds, \\
\mathbf{F}_I(\mathbf{B}_I) &= \oint_{\partial V} \mathcal{M}(\mathbf{B}_I) \cdot \mathbf{n} \, ds,
\end{aligned}$$

then we can see the difference between the MST and GMST is equivalent to the addition of two terms that analytically go to zero — interestingly appearing in the GMST derivation (13).

All analytic magnetic field solutions contain a singularity due to the Green's function ($1/r$, m⁻¹) when the field point is equal to the source point (this materialises in the definite integral limits, on the boundary of the source). Therefore, the analytic solutions contain discontinuities of \mathbf{B} inside the closed region that need to be removed for (8) to be applied. This is a topic covered in literature [28], and it can be shown that ignoring the singularities has no impact on a final solution. Similarly, the singularities have no effect on the solution using the GMST (20), with a brief discussion given in Appendix B.

Whilst the GMST $\mathcal{F}(\mathbf{B}_I, \mathbf{B}_E)$ is presented in this article using the internal and external vector fields, this is an arbitrary distinction and in general we have the solution

$$\mathbf{F}_{\text{GMST}} = \oint_{\partial V} \mathcal{F}(\mathbf{B}_1, \mathbf{B}_2) \cdot \mathbf{n} \, ds, \quad (22)$$

that can be extended to the force on the n th collection of magnetic sources from any number N of total collections of magnetic objects:

$$\mathbf{F}_{\text{GMST}_n} = \sum_{i=1}^N \oint_{\partial V} [\mathcal{F}(\mathbf{B}_n, \mathbf{B}_i) - \delta_{ni} \mathcal{F}(\mathbf{B}_n, \mathbf{B}_i)] \cdot \mathbf{n} \, ds. \quad (23)$$

3.3. The torque tensor

To calculate the torque we have a radius vector \mathbf{r} acting on the local force distributions from $\mathbf{B}_E(\mathbf{r})$ and $\mathbf{B}_I(\mathbf{r})$ on ∂V (B.4). From (14), the torque \mathbf{T} is defined

$$\mu_0 \mathbf{T} = \mu_0 \int_V \mathbf{r} \times \mathbf{f} \, dv = \int_V \mathbf{r} \times [(\nabla \times \mathbf{B}_E) \times \mathbf{B}_I + (\nabla \times \mathbf{B}_I) \times \mathbf{B}_E] \, dv. \quad (24)$$

Analogous to (19), with the divergence theorem identity (17), (24) becomes

$$\mu_0 \mathbf{T} = \oint_S \left(-[(\mathbf{B}_E \otimes \mathbf{B}_I + \mathbf{B}_I \otimes \mathbf{B}_E) \times \mathbf{r}] \cdot \mathbf{n} + [(\mathbf{B}_I \cdot \mathbf{B}_E) \mathbf{r}] \times \mathbf{n} \right) ds, \quad (25)$$

where the tensor is symmetrical in \mathbf{B}_I and \mathbf{B}_E . The vector and tensor components in (25) can be combined to give a single tensor that has a dot product with the normal:

$$\mu_0 \mathbf{T} = \oint_S \left[\left(-(\mathbf{B}_E \otimes \mathbf{B}_I + \mathbf{B}_I \otimes \mathbf{B}_E) \times \mathbf{r} + (\mathbf{B}_I \cdot \mathbf{B}_E) (\mathbf{e} \cdot \mathbf{r}) \right) \cdot \mathbf{n} \right] ds. \quad (26)$$

With $\mathbf{r} = x \mathbf{e}_x + y \mathbf{e}_y + z \mathbf{e}_z$ we get the GMST torque

$$\mathbf{T}_{\text{GMST}}(\mathbf{r}, \mathbf{B}_E, \mathbf{B}_I) = \oint_S \mathcal{T}(\mathbf{r}, \mathbf{B}_E, \mathbf{B}_I) \cdot \mathbf{n} \, ds, \quad (27)$$

in form of (20), with the torque tensor

$$\mathcal{T}(\mathbf{r}, \mathbf{B}_E, \mathbf{B}_I) = \frac{1}{\mu_0} \begin{bmatrix} \mathcal{T}_{11} & \mathcal{T}_{12} & \mathcal{T}_{13} \\ \mathcal{T}_{21} & \mathcal{T}_{22} & \mathcal{T}_{23} \\ \mathcal{T}_{31} & \mathcal{T}_{32} & \mathcal{T}_{33} \end{bmatrix},$$

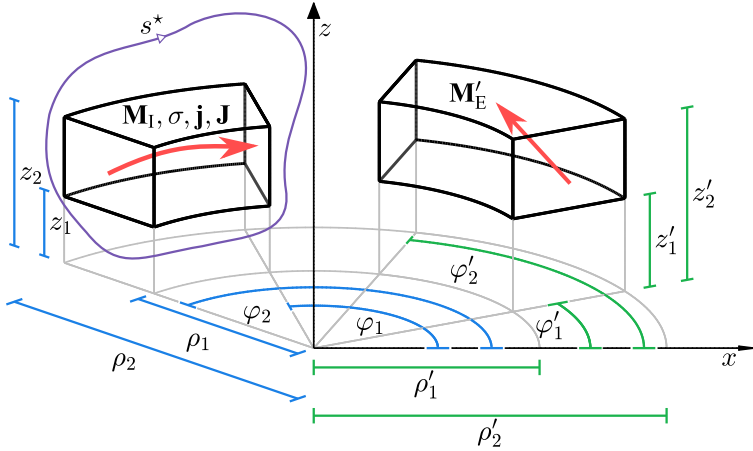


Figure 2: Parameterisation of two coaxial rectangular cylindrical sectors. The force between them is dependent on model, calculated either directly on the magnetic sources of one sector (blue, unprimed coordinates), or through a closed surface containing one of the sectors (purple, starred coordinates).

$$\begin{aligned}
 \mathcal{T}_{11} &= y(B_x^E B_z^I - B_z^E B_x^I) - z(B_x^E B_y^I + B_y^E B_x^I), \\
 \mathcal{T}_{22} &= z(B_x^E B_y^I + B_y^E B_x^I) - x(B_y^E B_z^I - B_z^E B_y^I), \\
 \mathcal{T}_{33} &= x(B_y^E B_z^I - B_z^E B_y^I) - y(B_x^E B_z^I + B_z^E B_x^I), \\
 \mathcal{T}_{12} &= y(B_y^E B_z^I + B_z^E B_y^I) + z(B_x^E B_x^I - B_y^E B_y^I + B_z^E B_z^I), \\
 \mathcal{T}_{13} &= -z(B_y^E B_z^I + B_z^E B_y^I) - y(B_x^E B_x^I + B_y^E B_y^I - B_z^E B_z^I), \\
 \mathcal{T}_{21} &= -x(B_x^E B_z^I + B_z^E B_x^I) + z(B_x^E B_x^I - B_y^E B_y^I - B_z^E B_z^I), \\
 \mathcal{T}_{23} &= z(B_x^E B_z^I + B_z^E B_x^I) + x(B_x^E B_x^I + B_y^E B_y^I - B_z^E B_z^I), \\
 \mathcal{T}_{31} &= x(B_x^E B_y^I + B_y^E B_x^I) - y(B_x^E B_x^I - B_y^E B_y^I - B_z^E B_z^I), \\
 \mathcal{T}_{32} &= -y(B_x^E B_y^I + B_y^E B_x^I) - x(B_x^E B_x^I - B_y^E B_y^I + B_z^E B_z^I).
 \end{aligned}$$

It is noted that whilst having completed the torque tensor derivation using the divergence identity, an equivalent result can be realised directly

$$\mathcal{T}(\mathbf{r}, \mathbf{B}_E, \mathbf{B}_I) = \mathbf{r} \times \mathcal{F}(\mathbf{B}_E, \mathbf{B}_I), \quad (28)$$

using the cross product between a tensor and a vector defined earlier; hence,

$$\mathbf{T}_{\text{MST}}(\mathbf{r}, \mathbf{B}) = \oint_S \mathbf{r} \times [\mathcal{M}(\mathbf{B}) \cdot \mathbf{n}] d\mathbf{s}. \quad (29)$$

4. Computational methods

This section summarises the technical details used to generate the results for all case studies in Sections 5 and 6, to be used in combination with details in the individual figure captions. All field solutions used in this article are from cylindrical geometries with uniform current or magnetisation. In the case of iron segments, these are represented as a matrix of magnetisations.

A general parameterisation is given in Figure 2 for the following discussion. Analytic magnetic field equations provide a solution at an unprimed point $\mathbf{r}(\rho, \varphi, z)$, found by integration of a bound distribution $\mathbf{M}'(\mathbf{r}, \mathbf{r}')$ at primed points $\mathbf{r}'(\rho', \varphi', z')$, with relative distances between the two $|\mathbf{r} - \mathbf{r}'|$ in a fixed Cartesian base. The integration limits are the parameterisation of the geometry, that in this article are all with respect to cylindrical parameters: $\rho' \in [\rho'_1, \rho'_2]$, $\varphi' \in [\varphi'_1, \varphi'_2]$, $z' \in [z'_1, z'_2]$. Analytic force calculations require integration of the magnetic field points through a second bound distribution $\mathbf{M}(\mathbf{r}, \mathbf{r}')$ that has a similar parameterisation: $\rho \in [\rho_1, \rho_2]$, $\varphi \in [\varphi_1, \varphi_2]$, $z \in [z_1, z_2]$. For the semi-analytic Lorentz methods herein (2), the magnetisation resolves into surface distributions of charge ($\sigma = \mathbf{M} \cdot \mathbf{n}$) or current ($\mathbf{j} = \mathbf{M} \times \mathbf{n}$); this reduced region is possible for all principal uniform magnetisations, whereby either the volumetric curl or divergence of the magnetisation is zero, dependent on model [33, §5.0]. Thus, the relevant

integral discretisations are:

$$\mathbf{F}_{\text{Charge}} = \sum_n \sigma^{(n)} \mathbf{B}_E^{(n)} s^{(n)}, \quad (30)$$

$$\mathbf{F}_{\text{Current}} = \sum_n \mathbf{j}^{(n)} \times \mathbf{B}_E^{(n)} s^{(n)}, \quad (31)$$

$$\mathbf{F}_{\text{Filament}} = \sum_n \mathbf{J}^{(n)} \times \mathbf{B}_E^{(n)} v^{(n)}. \quad (32)$$

For the MST and GMST, the unprimed coordinates are not representative of the discretised region on $\{\sigma, \mathbf{j}, \mathbf{J}\}$, but the location of internal magnetic field sources \mathbf{M}_I . An arbitrary surface s^* defines this distinction against external magnetic field sources \mathbf{M}_E , that are otherwise the sources of \mathbf{B}_E in the Lorentz model, thus the discretisations are:

$$\mathbf{F}_{\text{MST}} = \sum_n \mathcal{M}(\mathbf{B}_E^{(n)} + \mathbf{B}_I^{(n)}) \cdot \mathbf{n}^{(n)} s^{*(n)} \quad (33)$$

$$\mathbf{F}_{\text{GMST}} = \sum_n \mathcal{F}(\mathbf{B}_E^{(n)}, \mathbf{B}_I^{(n)}) \cdot \mathbf{n}^{(n)} s^{*(n)}. \quad (34)$$

For all discretisations an approximate 1:1 (cylindrical or Cartesian) linear spaced mesh is maintained in each mesh refinement. An optimal meshing algorithm is out of the scope of this article, although metrics are shown in Section 5 that can be used in a mesh refinement process. Results are compared to FEA (in Maxwell 2D or 3D, within the ANSYS Electronics Desktop 2022 R1: ANSYS, Inc., Canonsburg, PA, USA), that has an optimised meshing algorithm, and is a typical method in the literature for independently verifying an analytic integral formulation. The analytic and semi-analytic results are run using Mathematica (V12, Wolfram Research, Inc., Champaign, IL, USA) code that is not optimised for speed – our foremost focus is on the results being correct, yet the user can expect a significant improvement in the computational speeds shown with vectorisation techniques. All computations were completed on the same standard desktop PC (3.5 GHz processor E3-1240v5 and 16 GB RAM DDR4).

Normalised values for the force and torque are centered around 0 with a percent difference, e.g.

$$\bar{F}_{\text{Analytic}} = \frac{F}{F_{\text{Analytic}}} - 1 \quad (35)$$

referenced to an analytic result, or otherwise ($\bar{F}_{\text{Filament}}, \bar{F}_{\text{GMST}}, \bar{F}_{\text{FEA}}$).

Both the MST and GMST use the same field points and hence magnetic field values. Therefore, there is almost no additional computational overhead to always compute both force and torque results together for comparison.

5. Analytic comparison between the stress tensors

The advantage of using the GMST instead of the MST will be highlighted in three simple case studies that have analytic solutions:

- force between two axially magnetised permanent magnets;
- force between an axially magnetised permanent magnet and a coil with azimuthal current, modelled with a discrete number of filaments; and
- force on a three-phase filamental coil array within a Halbach PM array.

In a counter example, there is an additional case study with a solid coil, showing a potential downside to both the GMST and MST compared to Lorentz.

5.1. Magnetic spring

The first case study examined comprises a simple magnetic spring containing two axially magnetised and coaxial cylindrical permanent magnets, where $\mathbf{F} = F_z \mathbf{e}_z$. The magnets have an axisymmetric magnetic flux density, thus only a 2D mesh is required; however, for demonstration we also compute the force using a non-axisymmetric 3D mesh. Figure 3 shows results for the spring restoring force, where the convergence rates for the 2D and 3D discretisations are similar, albeit 3D requires two orders of magnitude more mesh elements. The highlight is that as the relative magnitude of potential energy between the magnets increases ($\mathbf{M}'_E : \mathbf{M}_I$), the MST has increased mesh inaccuracy whereas the GMST remains unchanged. In such linear systems (double the PM strength, double the force) then using the MST is not going to be a scalable solution, if for example, we are using an invariant mesh in a parametric study.

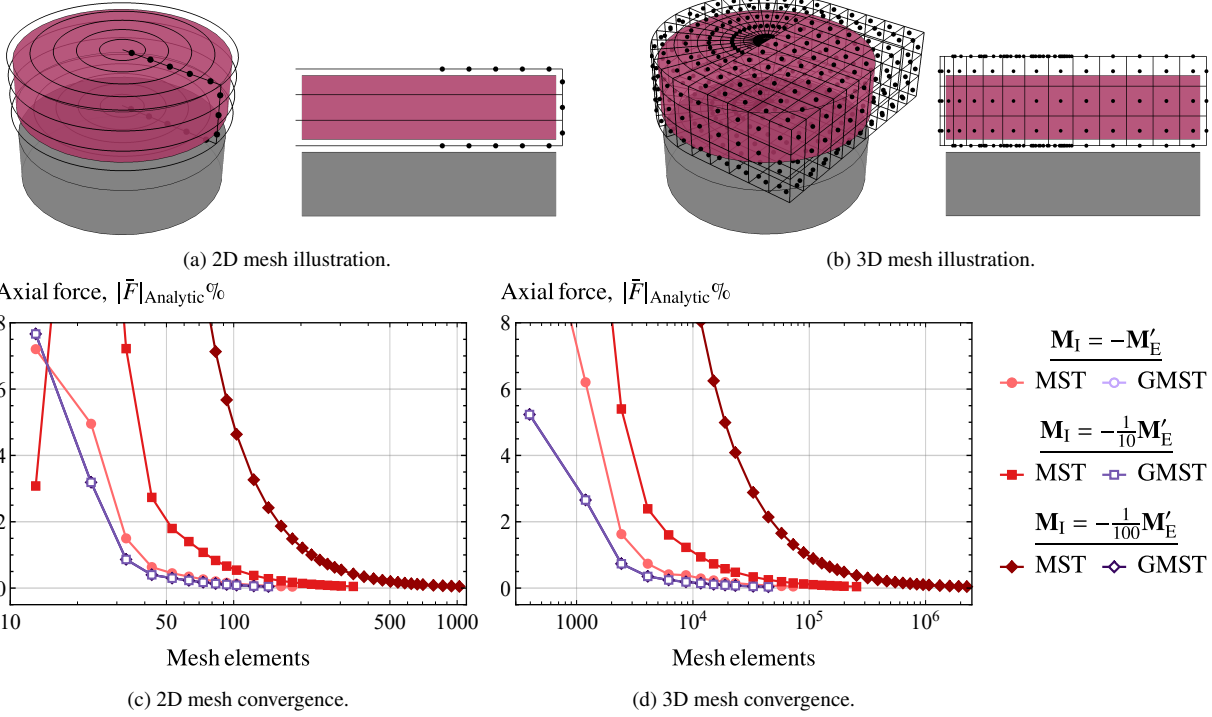


Figure 3: The axial force between two permanent magnets with axial magnetisations calculated with the MST and GMST tensors, normalised to the analytic results of $F_z = \{45.42 \text{ N}, 4.542 \text{ N}, 0.4542 \text{ N}\}$ for $\{\mathbf{M}_I, \frac{1}{10} \mathbf{M}_I, \frac{1}{100} \mathbf{M}_I\}$ respectively. The data points cease once converged to within 0.05 % of the analytic result. The magnets oppose with $-\mathbf{M}'_E = 955 \text{ kA}\cdot\text{m}^{-1} \mathbf{e}_z$ in $\rho = \rho' \in [0, 10] \text{ mm}$, $\varphi = \varphi' \in [0, 2\pi] \text{ rad}$, $z \in [6, 11] \text{ mm}$, and $z' \in [0, 5] \text{ mm}$. The analytic force between the cylindrical permanent magnets is given in [33, §6.3], with magnetic fields given in [33, §5.4].

The difference highlighted between the GMST and MST in Figure 3 is explained entirely by the external (magnetic field) force \mathbf{F}_E in the 2D case, that is independent of \mathbf{M}_I . This external force relative to the total MST force is shown in Figure 4a with a modified normalisation to (35):

$$\left(\frac{F_{\text{GMST}_z}}{F_{\text{Analytic}_z}} - 1 \right) = \left(\frac{F_{\text{MST}_z}}{F_{\text{Analytic}_z}} - 1 \right) - \left(\frac{F_E + F_I}{F_{\text{Analytic}_z}} \right), \quad (36)$$

based upon the analytic expression $F_{\text{GMST}} = F_{\text{MST}} - F_E - F_I$ (21). The differing normalisation of each term in (36) is required for comparison on an equivalent axis scale, as \mathbf{F}_E and \mathbf{F}_I will approach zero and not F_{Analytic_z} ; all bracketed terms will go to zero with increasing mesh, assuming no field error.

The scale of \bar{F}_E relative to \bar{F}_{MST} increases as \mathbf{M}_I decreases – the error due to \mathbf{F}_E being as large as \mathbf{F}_{MST} with $\frac{1}{100} \mathbf{M}_I$. Any errors due to discretisation of the internal (magnetic field) force \mathbf{F}_I cancel out when the mesh is symmetrically spaced about the permanent magnet due to field symmetry and opposite surface normals. This case is shown in Figure 3a with the 2D mesh illustration, whereas the 3D mesh deliberately induces possible errors without radial or axial symmetry. Error from this internal force is shown in Figure 4b, and scales inversely to the external force — the error due to \mathbf{F}_I being as large as \mathbf{F}_E with $\mathbf{M}_I = \mathbf{M}'_E$, but reduces as \mathbf{M}_I decreases.

More generally, the meshing error is linked to the change in magnetic flux through the closed surface as the mesh is refined. This can be quantified using both the normal and tangential components of the field as both tensors have a force related to the curl of the field along with addition of the ‘analytically zero’ divergence term(s). Using the divergence theorem ($\nabla \cdot \mathbf{B}$ terms) and a curl corollary ($\nabla \times \mathbf{B}$ terms) we have the average flux densities (or field error)

$$\langle \mathbf{B} \rangle_{\text{Div}} = \frac{1}{A} \left| \oint_S \mathbf{B} \cdot \mathbf{n} \, ds \right|, \quad (37)$$

$$\langle \mathbf{B} \rangle_{\text{Curl}} = \frac{1}{A} \left| \oint_S \mathbf{n} \times \mathbf{B} \, ds \right|, \quad (38)$$

normalised by the total surface area A of s^* , giving $\langle \mathbf{B} \rangle$ in units T or $\text{Wb}\cdot\text{m}^{-2}$ where $\langle \mathbf{B} \rangle = \langle B_\rho \rangle \mathbf{e}_\rho + \langle B_\varphi \rangle \mathbf{e}_\varphi + \langle B_z \rangle \mathbf{e}_z$. The divergence should go to zero (37) and the curl (38) should go to a constant as we have a non-zero \mathbf{J} in the enclosed region. Otherwise, the region would seemingly contain a magnetic monopole or have current passing through the surface, with the sign implying polarity or direction. To plot $\langle \mathbf{B} \rangle_{\text{Curl}}$, the average field error from the finest mesh calculated (a ‘converged’ value, or final value) is subtracted from all coarser meshes to give $\langle \bar{\mathbf{B}} \rangle_{\text{Curl}}$, such that the difference approaches zero along with $\langle \mathbf{B} \rangle_{\text{Div}}$.

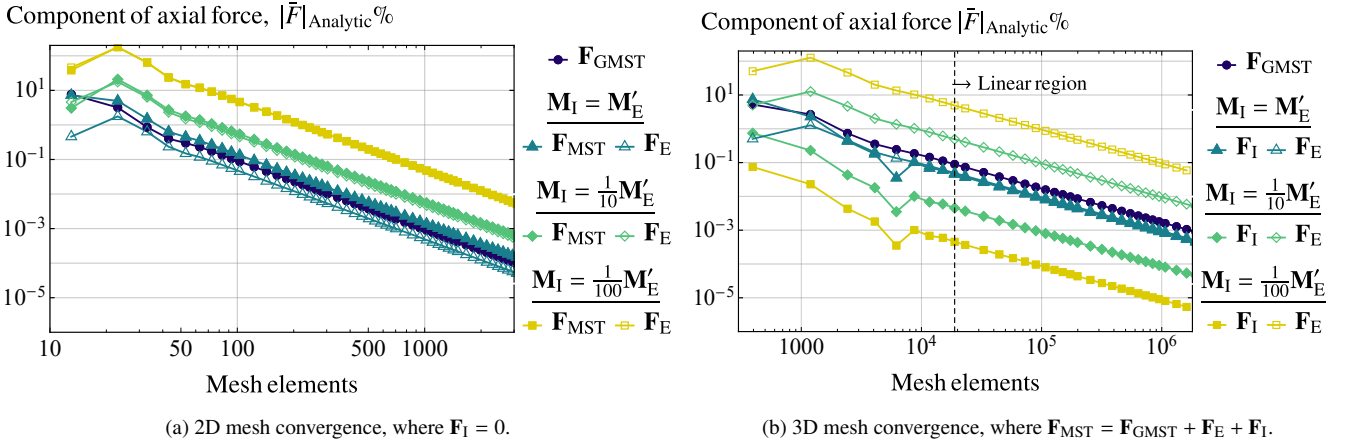


Figure 4: As the mesh is refined in the 2D and 3D cases of Figure 3, the ‘analytically zero’ tensor components in the MST ($\mathbf{F}_I, \mathbf{F}_E$) are the difference to the GMST. These results are extracted using (21).

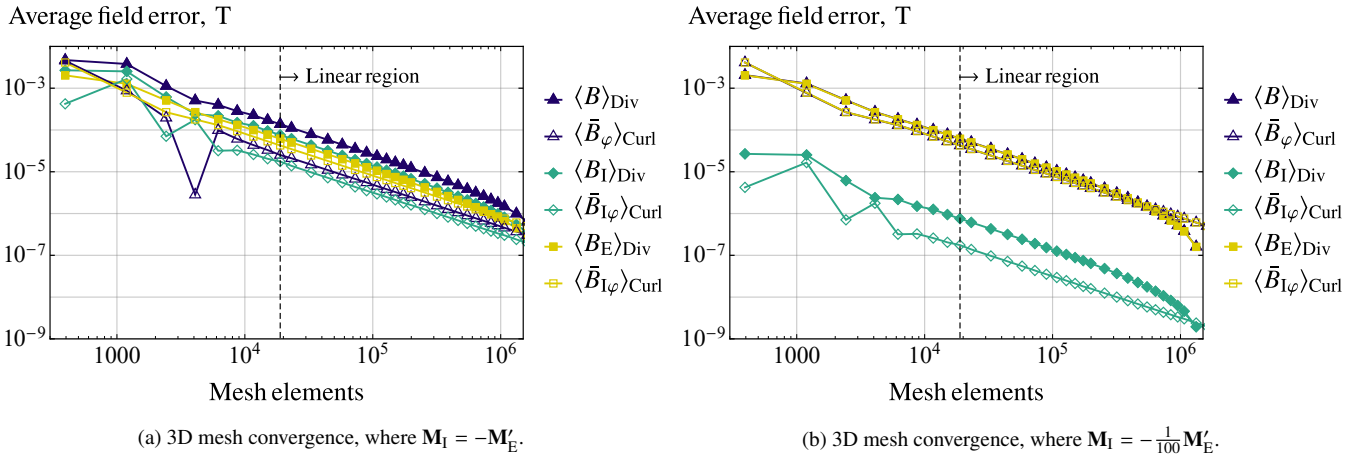


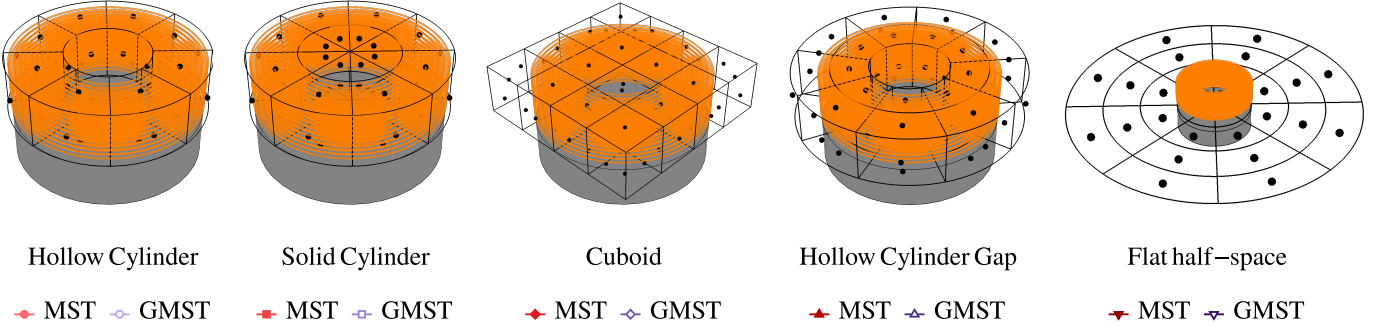
Figure 5: Quantification of the discretisation error in Figure 3d and Figure 4b, for volumetric error terms $\langle B \rangle_{\text{Div}}$ (37) and $\langle B \rangle_{\text{Curl}}$ (38) via tangential and normal components of the magnetic flux density across the closed integration surface. These are split into error contributions to the field from external and internal sources where $\langle B \rangle = \langle B_I \rangle + \langle B_E \rangle$. Further detail is shown in Figure C.1, Appendix C.

Components of $\langle \bar{B} \rangle_{\text{Curl}} = \langle \bar{B}_\varphi \rangle_{\text{Curl}} \mathbf{e}_\varphi$ and $\langle B \rangle_{\text{Div}}$ from internal and external sources are shown in Figure 5, where a linear log-log relationship can be seen between the field error and mesh elements, matched in Figure 4b. This shows, with sufficient mesh elements, a power law relationship between the force and average field errors — this gives confidence that, in this case study, with increasing mesh density the semi-analytic result will approach the analytic value in both 2D and 3D meshes, albeit at a reducing rate. The aforementioned subtraction of the final value of $\langle B_\varphi \rangle_{\text{Curl}}$ causes the appearance of rapid convergence at finer meshes. Figure 5a and Figure 5b highlight the change in average field errors with the scale of \mathbf{M}_I that the GMST is invariant to.

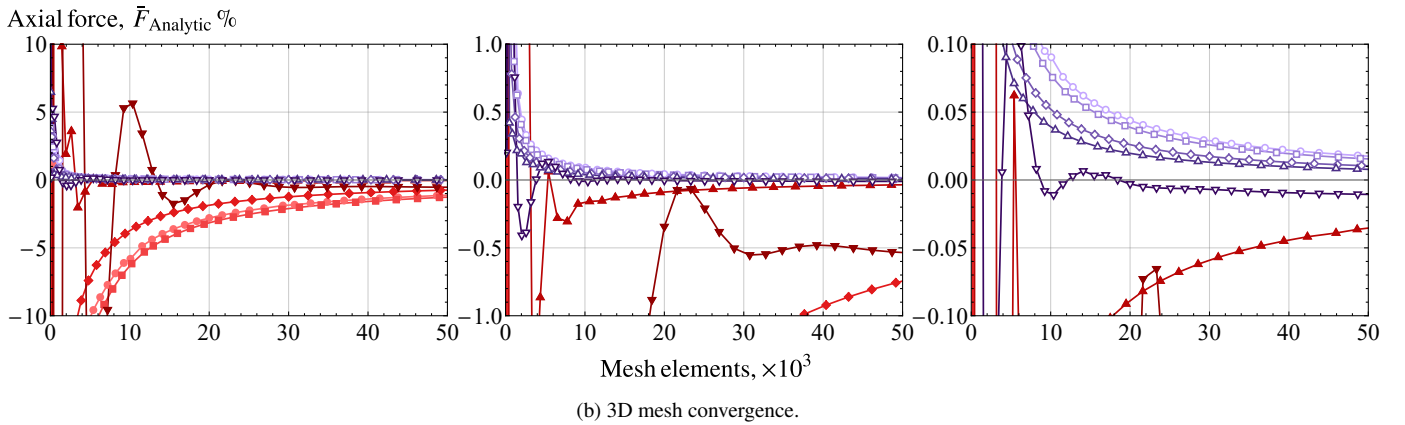
5.2. Magnetic actuator

In Section 5.1, a high sensitivity to field errors from mesh discretisation was shown when using the MST, when given exact field values. When not given exact field values, it will be shown the MST will amplify this introduced error. Firstly though, we will look at the sensitivity of the GMST and MST to a change in mesh geometry. In the second case study investigated, the upper magnet in the magnetic spring has been replaced with a coil, comprised of 100 turns, modelled as an equispaced grid of axisymmetric filaments with infinitesimal cross-sections. Figure 6 shows the actuation force on the coil, with comparison of four different closed surface meshes and one open surface mesh. The magnetic field from coils over an enclosing surface will typically be significantly lower than any surrounding (external) PM or iron segments, leading to significantly slower convergence rates in the MST due to a large \mathbf{F}_E component (as shown in the example Figure 4a). Overall, Figure 3 and Figure 6 shows that the GMST will have robust performance regardless of a chosen 2D or 3D mesh. Whereas care must be taken when choosing a closed surface mesh for the MST, with an example shown by the ‘Hollow Cylinder ’ and ‘Hollow Cylinder Gap ’ curves in Figure 6. A minor change to

the mesh radius of the outer cylindrical surface was made to show that the MST can produce results similar to the GMST; however, this is a manual process and in general the results are not robust.



(a) Mesh illustrations and corresponding plot legend for (b).



(b) 3D mesh convergence.

Figure 6: The axial force between a permanent magnet with axial magnetisation and a coil with azimuthal current, calculated using the MST and GMST, and normalised to the analytic result of $F_z = 0.55931$ N. The vertical axis is refined on each successive plot $\{\pm 10\%, \pm 1\%, \pm 0.1\%\}$ and results are shown for four different closed integration surfaces and one open integration surface, as illustrated in (a). The magnetisation is $\mathbf{M}_E' = 955 \text{ kA}\cdot\text{m}^{-1} \mathbf{e}_z$ in $\rho' \in [0, 10] \text{ mm}$, $\varphi' \in [0, 2\pi] \text{ rad}$, $z' \in [0, 5] \text{ mm}$. The coil current is $\mathbf{I} = 1 \text{ A} \mathbf{e}_\varphi$ in $\varphi \in [0, 2\pi] \text{ rad}$ per filament, placed at the centroids of circles of $\frac{1}{2} \text{ mm}$ diameter, square packed into $\rho \in [5, 10] \text{ mm}$, $z \in [6, 11] \text{ mm}$. The analytic force on the coil is given with $\sum_{i=1}^{100} \mathbf{F}_{\text{Filament}}^{(i)}$ from (2) with fields \mathbf{B}_E in [33, §5.4] and (for the semi-analytic force) \mathbf{B}_I in [33, §4.1].

It was discussed with Equation (6) that the force is entirely captured by the magnetic field in the airgap between sources, thus there is a lot of flexibility in choosing a mesh. The interesting example is the ‘Flat half-space’ in Figure 6, with the idea that an infinite plane would entirely capture the field. This is not exactly feasible with this semi-analytic method, yet we can consider a finite plane and assume most of the flux will pass through this. Theoretically, this assumes the missing surface(s), that would otherwise enclose the volume of the coil, have a zero normal magnetic field component and hence integrate to zero force contribution. Practically, there is flux leakage around the finite half-plane with a non-zero divergence in the tensor. The benefit to such an approach is a significantly simpler mesh giving potential for a lower computation time with the concession of introducing error into the result. With the specific case shown (plane radii $4.5 \times$ the outer PM radii) a monotonic convergence with the closed surface meshes is sacrificed for achieving the smallest number of mesh elements to get within 0.01% of the analytic result. Using unique meshes that introduce deliberate error is not practically feasible with the MST.

Continuing on from the half-space example, we consider not introducing error through the mesh, but in the field itself with $\mathbf{B}_E \rightarrow \mathbf{B}_E + \epsilon$. The axial force contribution from a mesh element is then

$$\begin{aligned} \mu_0 \frac{F_{\text{MST}z}^{(n)}}{s^\star} &= \mu_0 [\mathcal{M}(\mathbf{B}_E + \mathbf{B}_I + \epsilon) \cdot \mathbf{e}_z] \cdot \mathbf{e}_z \\ &= B_z^E B_z^I - B_x^E B_x^I - B_y^E B_y^I + \frac{1}{2} [(B_z^E)^2 + (B_z^I)^2 - (B_x^E)^2 - (B_x^I)^2 - (B_y^E)^2 - (B_y^I)^2] \\ &\quad + \epsilon (B_z^E + B_z^I - B_x^E - B_x^I - B_y^E - B_y^I) - \frac{1}{2} \epsilon^2 \end{aligned} \quad (39)$$

from (33) for the MST, and

$$\begin{aligned} \mu_0 \frac{F_{\text{GMST}z}^{(n)}}{s^\star} &= \mu_0 [\mathcal{F}(\mathbf{B}_E + \epsilon, \mathbf{B}_I) \cdot \mathbf{e}_z] \cdot \mathbf{e}_z \\ &= B_z^E B_z^I - B_x^E B_x^I - B_y^E B_y^I + \epsilon (B_z^I - B_x^I - B_y^I) \end{aligned} \quad (40)$$

from (34) for the GMST. A constant external field error ϵ will add a linear offset scaled by the internal field (and vice-versa) for the GMST. For the MST, this same field error adds a linear offset scaled to both the internal and external fields and an additional (possibly negligible) quadratic offset of the error. This gives the MST an inherent increased sensitivity to errors in the field. In cases where the internal field is small (or vice-versa with internal field error) then effects from the field error in the GMST will be minimal. The reason this is important is from the structure of analytic magnetic field solutions. When an analytic solution cannot be found in ‘closed-form’ or as a finite sum of special functions, it can be found as an exact infinite series. In practice, when using an infinite series solution there is a balance between accuracy and computational efficiency when choosing the number of terms to evaluate. There is spatial non-linearity with the location of the field point and the number of terms required for an expected field error; there will be varying error across all field points when evaluating an equal number of terms at all points. Not all contributions to the total field may be found via a series.

The impact to the force from error in the field due to a finite sum is thus difficult to predict, but as demonstrated with (39) and (40), these errors will be amplified by the MST relative to the GMST. The analytic magnetic field solution for a solid coil is complex, and expressed in-part by an infinite series. In the third case study, the discrete coil filaments are replaced with a solid current density. The values are normalised again using the filament force model; however, a converged value is used as this is a semi-analytic result with an increasing square discretisation through the axisymmetric coil cross-section. Figure 7 shows the actuation force over computation time for FEA and the two different semi-analytic methods, with differing 2D meshes. For the filament model with $J_\varphi \times 25 \text{ mm}^2 = 100 \text{ A}$ and a 10×10 square grid of points through the cross-section, the result will be identical to that in Figure 6 with $100 \times 1 \text{ A}$ turns; this discretisation effectively increases the number of filaments to capture the contour of \mathbf{B}_E across the coil. The converged result is different in this case study, albeit slightly.

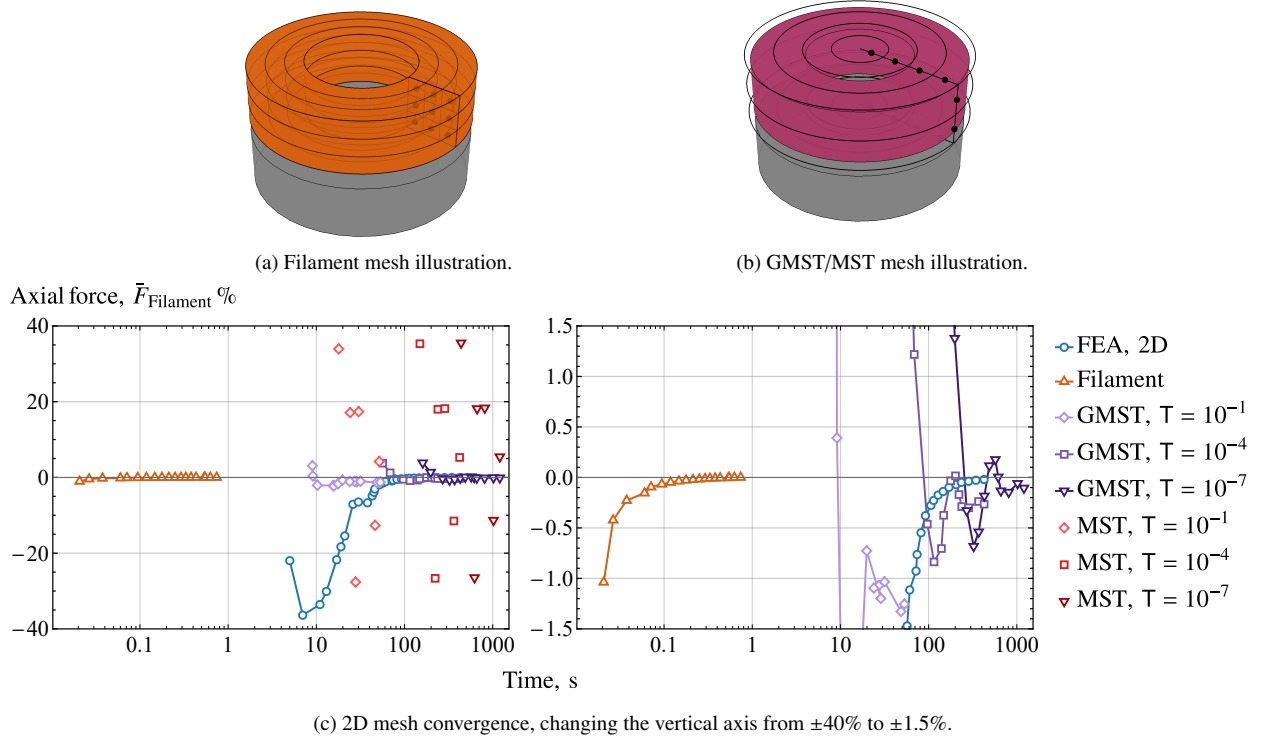


Figure 7: The axial force case study in Figure 6 is replicated with an axisymmetric mesh and solid coil $\mathbf{I} \rightarrow \mathbf{J} = 4 \text{ MA}\cdot\text{m}^{-2}\mathbf{e}_\varphi$, where the current density equates to an equivalent total current. The force is normalised to a ‘converged’ semi-analytic value of $F_z = 0.55947 \text{ N}$ using (32) with 400 volumetric segments. All non-mentioned specifications are equivalent to those listed in Figure 6, with field \mathbf{B}_I in [33, §4.4] calculated with decreasing tolerances T (a spatial tuning factor for the number of series terms calculated). Illustrations of the meshes are given in (c) with the filament on top and tensor on bottom.

The tensor results of Figure 7 highlight an extreme end of complexity for this simple actuator. Only the radial component of \mathbf{B}_E is required for the filament model, whereas radial and axial components of both \mathbf{B}_E and \mathbf{B}_I are required for the GMST and MST. On top of this, both analytic magnetic field components of the solid coil \mathbf{B}_I are expressed in-part by an infinite series, with the number of terms chosen by a tolerance parameter. This leads to a significant computation expense, on the order of magnitude with FEA; however, the code for the tensor calculation is far from optimised compared to FEA. Additionally the MST is highly inaccurate relative to the GMST, as predicted, with induced error from spatially variant finite sums. Most MST points do not fit within the plot, with no accuracy improvement when increasing the tolerance parameter, unlike with the GMST.

For context: the analytic magnetic spring calculation (Figure 3) took 0.3 ms, equivalent to 1 standard field point calculation [33, §5.1]; the analytic magnetic actuator calculation (Figure 6) took 0.24 s with 100 field point calculations (100 filaments) and

additional overhead; and, the semi-analytic filament model (Figure 7) got to within 0.1% of the final result in 0.06 s, with the 2D FEA model taking 170 s for an equivalent metric. These timing results indicate that in simple systems analytic solutions will always be preferred, yet semi-analytic solutions perform well when adding complexity to a model and are a significant improvement over FEA with a complete region mesh.

5.3. Linear motor

The magnetic spring and actuator case studies in Sections 5.1 and 5.2 are relatively simple, containing a single coil and/or magnet within the tensor surface. The final case study incorporates an axisymmetric PM Linear Synchronous Motor (PMLSM) that has multiple coil phases and varying PM magnetisations, as shown in Figure 8. This is a discrete section of an otherwise periodic structure, thus it contains end effects due to no assumption of periodicity in the boundary conditions. All basis vectors of \mathbf{B}_l in Figure 7 involve finite summations of infinite series analytic solutions, and every mesh point had a different number of terms computed. In this PMLSM case study, the axial magnetic field component of the radially magnetised PM contains in-part an infinite series, and we are computing the same number of terms at all field points for illustrative purposes (not a computationally efficient method due to spatially varied rates of convergence). With this constraint, it is expected the force result will become more accurate as the number of terms in the series increases. This is certainly the case with the GMST, converging to within 0.3% of the analytic result after 10 s with 10 terms, and improving thereafter. The MST has an inconsistent result, where as the number of terms increases from 10 to 25, the converged result goes from 1.3% error to 3%; the MST converges to finite non-zero values dependent on the model parameters.

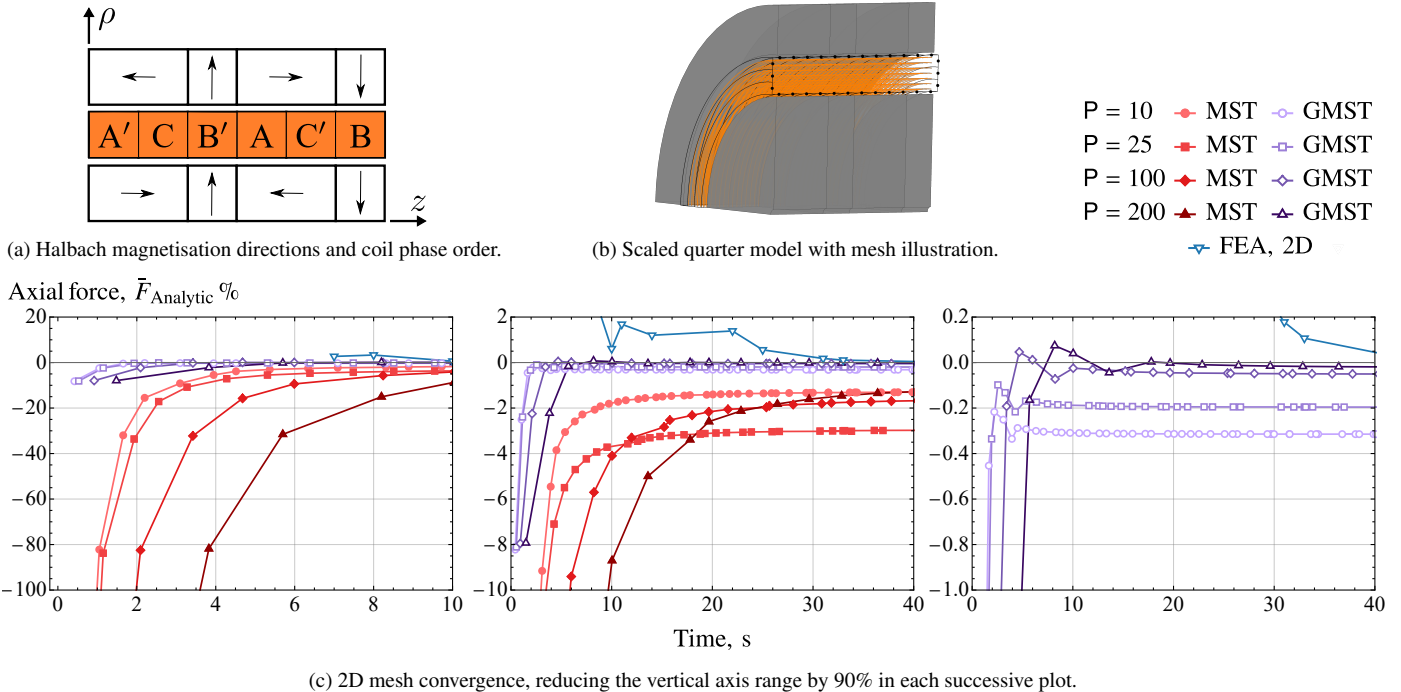


Figure 8: The axial force from a non-periodic PMLSM segment with a double-sided Halbach magnetisation and three-phase coil array. The coil cross-sections are separated by 60 electrical degrees, with three per pole pitch, and filament currents $\mathbf{I} : \{A', C, B', A, C', B\} = \{2, -2, -4, -2, 2, 4\}A \mathbf{e}_\varphi$ in $\varphi \in [0, 2\pi]$ rad. The filaments are placed at the centroids of circles 1 mm in diameter, square packed into $\rho \in [23, 30]$ mm, $z \in [6(i-1), 6i]$ mm for $i = 1 \rightarrow 6$. The magnetisation directions in (a) and equal magnitudes $|\mathbf{M}'_E| = 955 \text{ kA}\cdot\text{m}^{-1}$ in: inner array $\rho' \in [1, 22.5]$ mm; outer array $\rho' \in [30.5, 40]$ mm; $\varphi' \in [0, 2\pi]$ rad; radial PMs $z' \in [12, 18] \cup [30, 36]$ mm; axial PMs $z' \in [0, 12] \cup [18, 30]$ mm. The results from the tensors and FEA are normalised to an analytic result of $F_z = 63.459$ N, with the FEA model converging to $F_z = 63.467$ N with solid coils ($J = 4 \text{ M}\cdot\text{m}^{-2} \mathbf{I}$) versus filaments in the analytic and semi-analytic models. The analytic force on the coil is given with $\sum_{j=1}^{6 \times 42} \mathbf{F}_{\text{Filament}}^{(j)}$ from (2) with fields \mathbf{B}_E in [33, §5.2 & 5.4] with P terms in series and (for the semi-analytic force) \mathbf{B}_l in [33, §4.1].

As mentioned previously, semi-analytic force or torque solutions are dependent on the computational efficiency of the field equations. This was shown to detriment with the computationally expensive field equations from a solid coil compared to 2D FEA (Figure 7); however, as shown with Figure 8, the optimised (or practical) series solutions for the PM magnetic field, used with the GMST, compute significantly faster than FEA even when a high number of terms are used. The motor force is practically indifferent in this case study between a model with 1D filaments or a ‘stranded’ 3D volume in FEA. The solid coil can also be modelled as a series of 2D elements [38] with current sheet discs [33, §4.2] or shells [33, §4.3].

Figure 4 and Figure 5 quantify the error in the magnetic spring case study from discretisation of the exact magnetic field contour. From the linear motor case study, Figure 9 additionally quantifies the error due to minor inaccuracies in the magnetic field from computing a finite sum of an exact analytic infinite series solution. Instead of seeing a linear log-log relationship between error and mesh elements, the solution plateaus to a constant error offset for the total force and field divergence. Importantly, \mathbf{F}_E does not approach zero (and neither would \mathbf{F}_I with an asymmetric field and mesh). Minimal effect is seen in the curl due to small tangential field components on the closed surface from the radial PMs. Increasing the number of series terms from 25 to 200 reduces the average divergence field error (with 842 mesh elements) from 705 μT to 64 μT that: reduces the GMST force error from 0.31 % to 0.022 %; reduces the MST force error from 2.8 % to 0.95 %. The amplification of errors in the MST are significant and computationally expensive to resolve when infinite series solutions are used.

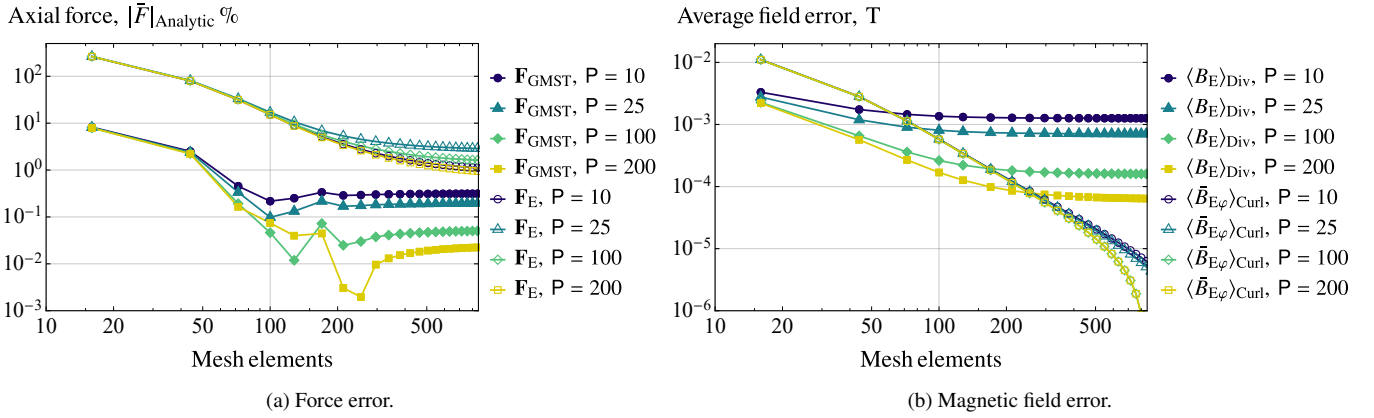


Figure 9: Analysis of mesh discretisation errors in Figure 8 with increasing series terms P for: (a) the total force using the GMST and ‘analytically zero’ MST term \mathbf{F}_E ; (b) the closed-surface external magnetic field split into normal $\langle B \rangle_{\text{Div}}$ and tangential components $\langle \bar{B} \rangle_{\text{Curl}}$. Further detail is shown in Figure C.2, Appendix C.

6. Numeric comparison between force models

A semi-analytic method may not be expected to perform better than an analytic solution when one is available, such as the axisymmetric 2D cases in Section 5. With more complex 3D geometries, analytic force solutions become difficult to derive and compute [33, §6.4], leading to questionable improvements over FEA or numeric integral methods — this is where semi-analytic solutions are most required. The focus in this section is a comparison using relatively ‘simple’ 3D geometries with cylindrical arc PMs, where FEA is significantly slower than the 2D cases. The axial force and torque on two different couplers are analysed, one with diametrically magnetised PMs, and one with axially magnetised PMs. This includes a comparison to the traditional charge (30) and current (31) semi-analytic force models that are expected to scale poorly with the number of mesh sources (Section 2.2). The linear motor case study of Section 5.3 is revisited to include soft magnets, that are modelled using a large number of PMs. As a final case study, Appendix D demonstrates use of the supplementary material that can calculate force and torque between any collection of magnets or coils used this article – useful toward reproduction of this work.

6.1. Force couplers with axial or radial flux

The radial and axial force couplers are chosen to include different surfaces of charge and current from different PM magnetisations. This is highlighted in the mesh illustrations of Figure 10 and Figure 12. In the charge model, the axially magnetised PMs are modelled as two discs of charge (Figure 11c), whereas the diametrically magnetised PMs are modelled on the orthogonal surfaces with two sections and shells of charge (Figure 13c). The mesh remains consistent between the charge current models, e.g. Figure 13d is the combination of the meshes of Figure 11c and Figure 11d. A single GMST/MST mesh is used in both case studies, testing consistency of the results to a variant (increasing 8, 16, 32 PMs) and contrasting (radial vs axial flux) magnetic field. The chosen mesh may not be optimal, but various meshes were tested in a single case study (Figure 6) that demonstrate the GMST is relatively insensitive to the mesh geometry.

Comparisons between the five methods are given in Figure 11 and Figure 13. There are relatively consistent results between the MST and GMST compared to the other methods. This is due to all the PMs having equal magnetisations without series magnetic field solutions, recalling the significant errors shown in Figure 3 and Figure 7. With more complex fields (Cartesian magnetisation on cylindrical surface), errors in the MST are amplified, seen in the force results across Figure 13a to Figure 13c. Both tensors scale better than the charge, current, and FEA models when increasing the number of magnetic elements – the charge and current models begin to perform poorly relative to FEA with 32 total PMs. With 8 total PMs and a coarse mesh, the charge and current models are the best performing for an approximate solution. For results requiring higher accuracy, the use of either tensor is a preferred computational method.

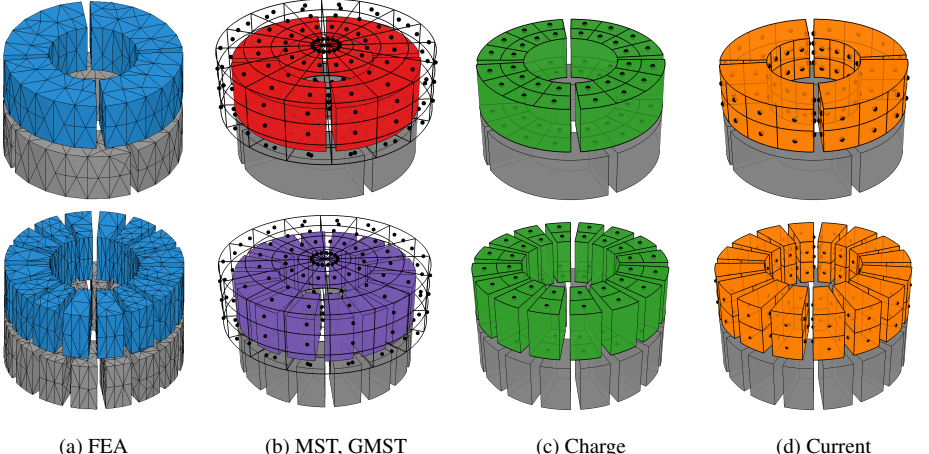


Figure 10: Alternative methods to calculate the force and torque on the upper (coloured) axially magnetised PMs with: a volume mesh in the entire region (a); and various semi-analytic surface meshes with significant mesh-free regions (b-d). Results are given in Figure 11.

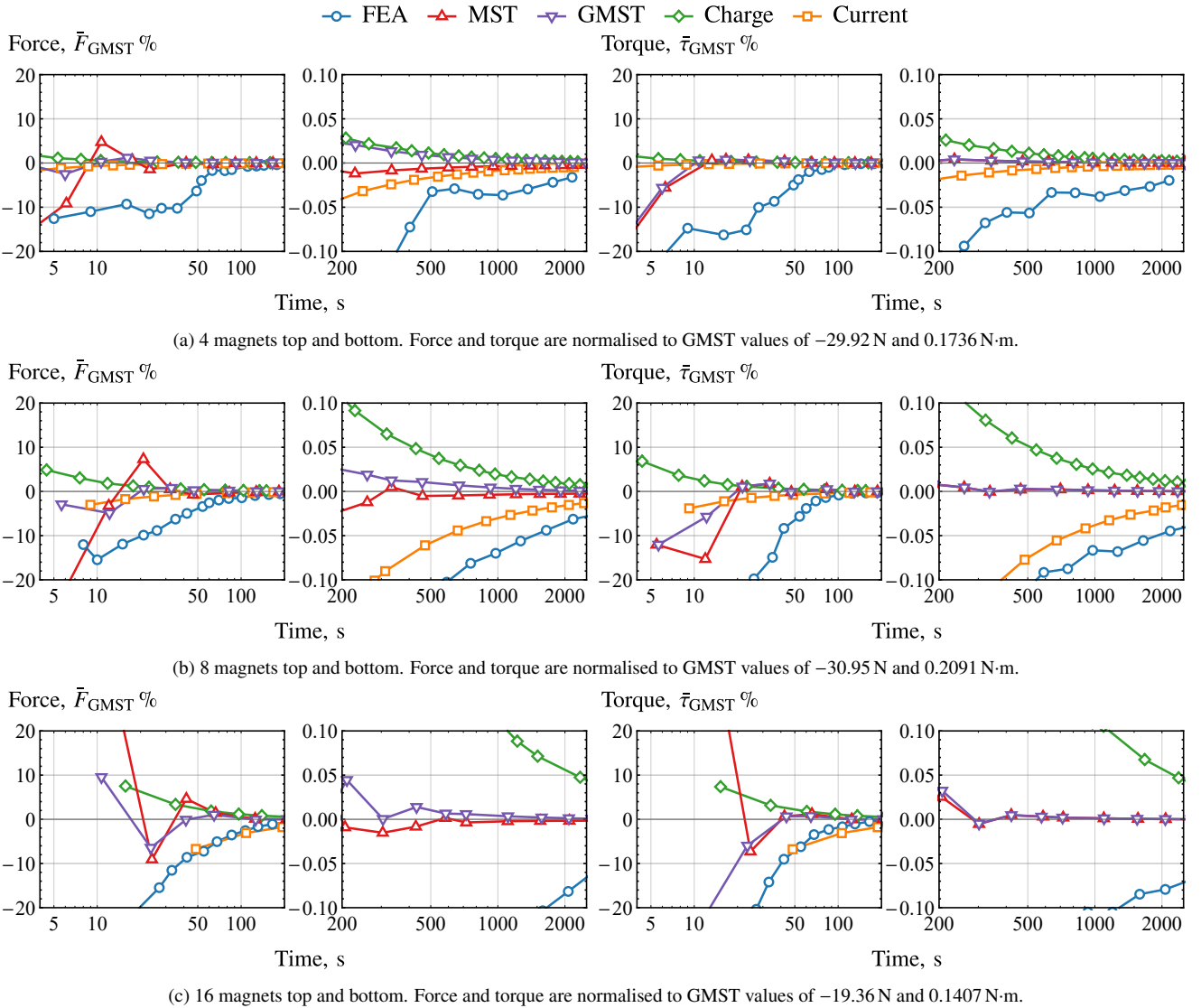


Figure 11: Axial force and torque values for an axial force coupler with axially magnetised permanent magnets are shown in (a-c). The plots compare FEA and different semi-analytical methods, increasing the number mesh elements in each plot and the number of magnets across plots. Illustrative surface meshes for the semi-analytic methods are shown in Figure 10 for $N = \{4, 8, 16\}$ magnets. The horizontal axis is split, changing the vertical axis from $\pm 20\%$ to $\pm 0.1\%$. The magnetisations alternate $\mathbf{M}_z^{(i)} = \mathbf{M}'_z^{(i)} = (-1)^i 955 \text{ kA/m} \mathbf{e}_z$ for $i = 1 \rightarrow N$, with a skew $\phi = \frac{\pi}{2N}$ and gap $\theta = \frac{\pi}{64}$. Magnet geometries are $\rho \in [5, 10] \text{ mm}$, $\varphi^{(i)} \in [\theta, \frac{2\pi}{N} - \theta] - \phi + \frac{2\pi}{N}(i-1) \text{ rad}$, $z \in [6, 11] \text{ mm}$ and $\rho' \in [5, 10] \text{ mm}$, $\varphi'^{(i)} \in [\theta, \frac{2\pi}{N} - \theta] + \frac{2\pi}{N}(i-1) \text{ rad}$, $z' \in [0, 5] \text{ mm}$. The semi-analytic forces on the coil are given by Equations (30,31,33,34) with fields \mathbf{B}_E and \mathbf{B}_I in [33, §5.4].

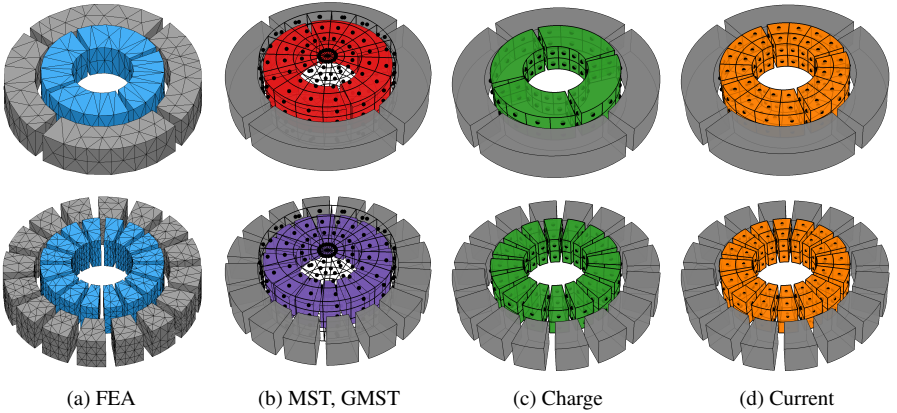
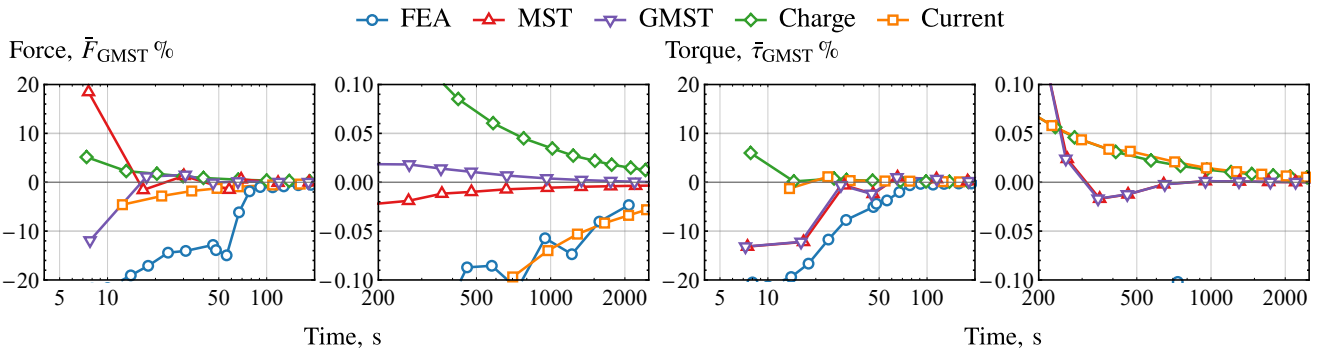
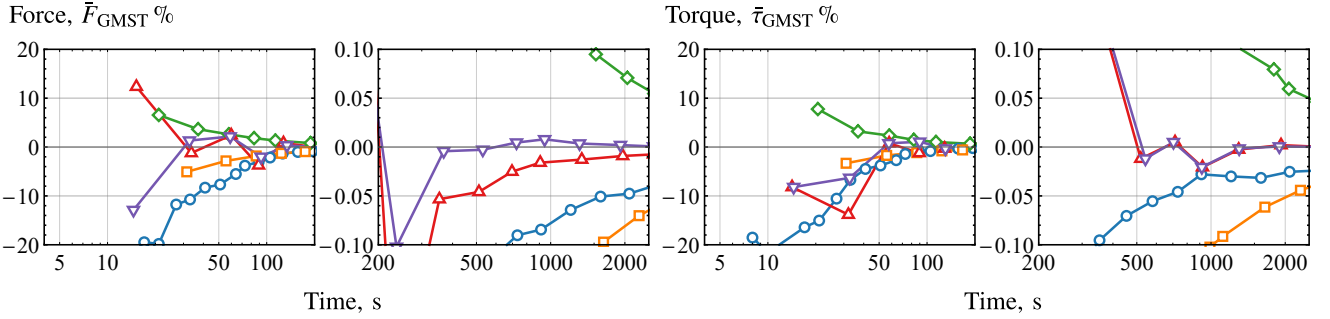


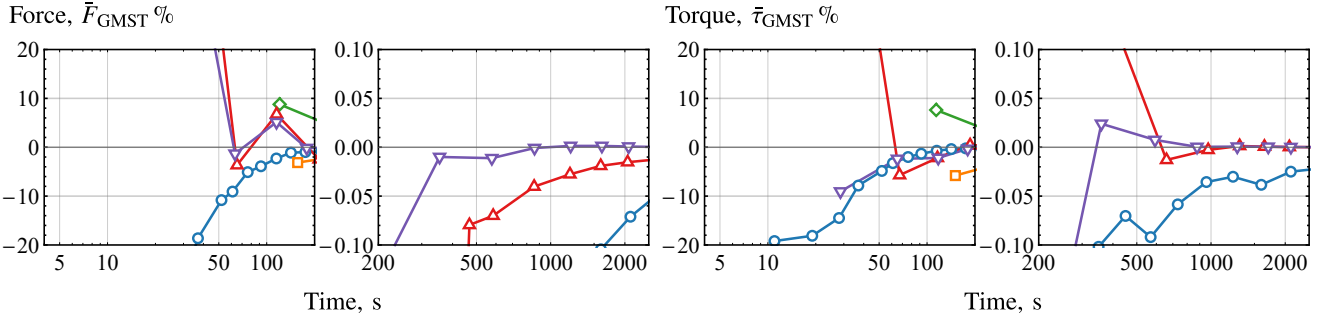
Figure 12: Alternative methods to calculate the force and torque on the inner (coloured) diametrically magnetised PMs with: a volume mesh in the entire region (a); and various semi-analytic surface meshes with significant mesh-free regions (b-d). Results are given in Figure 13.



(a) 4 magnets top and bottom. Force and torque are normalised to GMST values of -29.92 N and $0.1736 \text{ N}\cdot\text{m}$.



(b) 8 magnets top and bottom. Force and torque are normalised to GMST values of -30.95 N and $0.2091 \text{ N}\cdot\text{m}$.



(c) 16 magnets top and bottom. Force and torque are normalised to GMST values of -19.36 N and $0.1407 \text{ N}\cdot\text{m}$.

Figure 13: Axial force and torque values for a radial force coupler with diametrically magnetised permanent magnets is shown in (a-c). The plots compare FEA and different semi-analytical methods, increasing the number mesh elements in each plot and the number of magnets across plots. Illustrative surface meshes for the semi-analytic methods are shown in Figure 12 for $N = \{4, 8, 16\}$ magnets. The horizontal axis is split, changing the vertical axis from $\pm 20\%$ to $\pm 0.1\%$. The magnetisations alternate $\mathbf{M}_\perp^{(i)} = \mathbf{M}'_\perp^{(i)} = 955 \text{ kA/m} (\cos \varphi^{\star(i)} \mathbf{e}_x + \sin \varphi^{\star(i)} \mathbf{e}_y)$ for $i = 1 \rightarrow N$, with an angle $\varphi^{\star(i)} = \frac{1}{2}(\varphi_2 - \varphi_1) + \pi \operatorname{sgn}(1 + (-1)^{i+1})$, a skew $\phi = \frac{\pi}{2N}$, and gap $\theta = \frac{\pi}{64}$. Magnet geometries are $\rho \in [5, 10] \text{ mm}$, $\varphi^{(i)} \in [\theta, \frac{2\pi}{N} - \theta] - \phi + \frac{2\pi}{N}(i-1) \text{ rad}$, $z \in [\frac{5}{4}, \frac{21}{4}] \text{ mm}$ and $\rho' \in [11, 16] \text{ mm}$, $\varphi'^{(i)} \in [\theta, \frac{2\pi}{N} - \theta] + \frac{2\pi}{N}(i-1) \text{ rad}$, $z' \in [0, 5] \text{ mm}$. The semi-analytic forces on the coil are given by Equations (30,31,33,34) with fields \mathbf{B}_E and \mathbf{B}_I in [33, §5.1].

6.2. Linear motor with iron slots

We have demonstrated the scalability benefits realised using the tensors in complex 3D simulations, and the robustness of the GMST compared to the MST. To compound the sources of error using the MST (shown in Section 5), the axisymmetric 2D linear motor case study from Figure 8 is revisited with the incorporation of slots.

The addition of iron in a PMLSM (in the mover or stator) cannot be ignored as the inclusion can provide significantly higher peak forces from the variable magnetic reluctance. Also, $\approx 50\%$ higher magnetisations (at room temperature) are achievable in soft iron compared to the strongest permanent magnet [39], e.g. applications replacing the radial PMs in a Halbach array with iron [40], a pseudo-PM (where the iron segment has an approximately invariant magnetisation in operation). Iron sections have a nonlinear B - H curve, that to model effectively using linear PMs requires: discretisation to capture the magnetisation distribution from the external magnetic field; and iteration to capture the self-magnetisation. Details on the procedure are reproduced from [34] and found in Appendix A. Due to the large number of PMs required, the current and charge semi-analytic force models are not feasible.

There are now three refinements to consider in a model including iron:

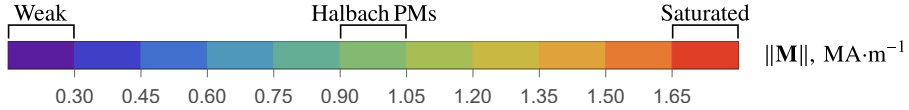
- discretisation of the closed surface mesh;
- discretisation of the iron into PM segments; and
- number of terms in any magnetic field series solution.

This is a difficult problem that we are not seeking to optimise in this article. For the intended application to motor design parametric studies, what is required is a computationally efficient method that can provide a good approximation of the solution using a coarse discretisation of the iron and mesh, and using a low number of series terms.

Figure 14 shows the magnetisation and force results of the PMLSM with a constant low number of terms for the radial PMs ($P = 10$) and increasing mesh discretisation, starting from a coarse iron discretisation (8 PMs) with manual refinement (20, 36 PMs). Relative permeability data for each iron segment (radial and axial PMs) from Figure 14d is overlaid on Figure A.1, showing the elements are operating along the full B - H curve. If a constant relative permeability was assumed, this would significantly differ to the material data across the radial and axial components. The analytic result (Figure 14f) is normalised to the FEA result that is a reasonable reference; however, both models are not strictly equivalent. The FEA model has a solid coil, not filaments, and interpolation methods for the B - H curve differ between the analytic code and FEA software. The GMST coarse iron discretisation differs to FEA by 1.1%, and the finer 36 PM iron discretisation differs by 0.6%. This is a great preliminary result, yet it is noted that increasing iron discretisation has an exponential computation expense, that is the primary limitation of this linearisation method. For the 8 PM segmentation, there are 96 PMs modelling the iron (axial plus radial), with the magnetic field calculated from each PM on all 48 PMs centroids. As the iron segments self-magnetise, this is a process that (depending on the relative permeability) takes ≈ 20 -50 iterations. That is already a computation time range of 28 s to 69 s if each field point takes 0.3 ms (without optimised code or specialist hardware). The GMST and MST results have an $\approx 3\%$ variance, that will lead to significantly different linearisations of the nonlinear iron slots.

Due to so many interactions between PM segments, it is very important not to calculate too many terms in a magnetic field series. This problem has been addressed for the radial PM in [33, §3.5], whereby knowing the series limit provides a maximum remainder R , thus all field points can be calculated with an algorithm for a uniform spatial error convergence. This spatial series convergence can be visualised in Figure 15 for a single radial PM, where some regions may only require the first term, and narrow regions require many. It is clear that using a constant number of terms spatially, as done in Figure 8c and Figure 14f, is computationally inefficient. Using the algorithm will minimise the MST error across the mesh; however, for computational efficiency we still need to truncate the maximum number of terms in each series.

For the single coil position examined in this particular case study, we now have an idea for the appropriate number of series terms, mesh discretisation, and iron discretisation. For a complete study we require this result to be robust over a range of permutations. This is demonstrated in Figure 16 with varying displacements used to calculate force over the stroke, whereby close tracking with FEA is seen in the GMST solution. From Table 1, the mean absolute relative difference with FEA for all points is 2.2% – 2.8% for the GMST discretisations and 6.8% – 7.6% for the MST. Comparing the MST to the GMST across the full stroke, the mean absolute relative difference is 7.6% for 8 PM and 5.7% for 36 PM. The result is also shown for no iron (or iron with unity relative permeability) – where this intersects the other curves is when the reluctance force is net zero (stable point with no coil current). This iron reluctance force is shown in Figure 17 for the ‘periodic’ section, between the vertical dashed lines in Figure 16c, removing the regions containing significant end effects. The MST results improve from $\approx 3\times$ the FEA to GMST difference down to $\approx 2\times$, where the force contribution from the coils is similar to the reluctance – highlighting again the MST issue with modelling contrasting strength fields (Figure 3). With lower coil currents and/or larger reluctance forces, the MST will perform more poorly. There are notable visual differences comparing the MST solution with FEA, in both peak forces and the general force profile. There are no numerical artefacts using the GMST, and this basic linearisation using analytic magnetic field solutions captures the complete nonlinear problem under a range of perturbations. The analytic magnetic field equations combined with the GMST provide a robust solution to the motor design parametric study requirements.



(a) A colourmap of the normalised PM magnetisations in (b-d). The iron slots between the coil phases are modelled by discretisation of PMs with a uniform magnetisation, ranging from weakly magnetised <0.38 T to saturated ≈ 2.07 T, with the Halbach PMs at ≈ 1.2 T. Further detail is provided in Appendix A.

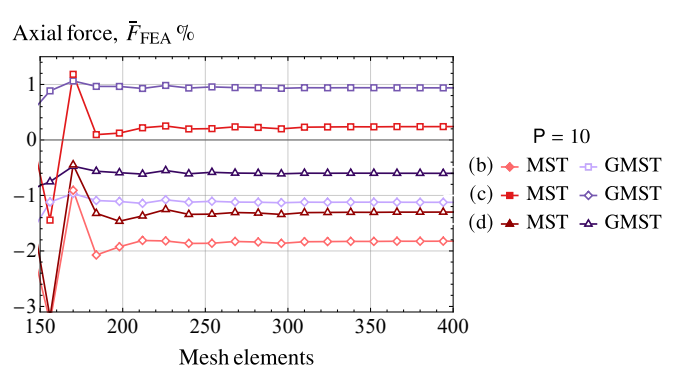
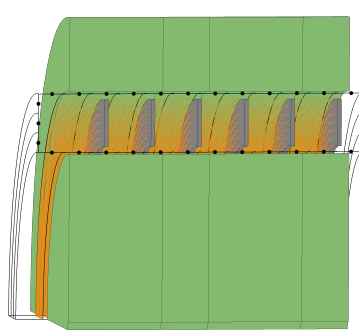
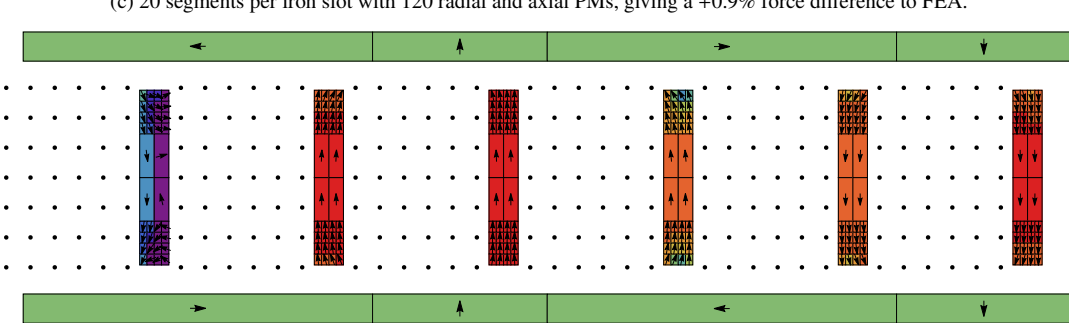
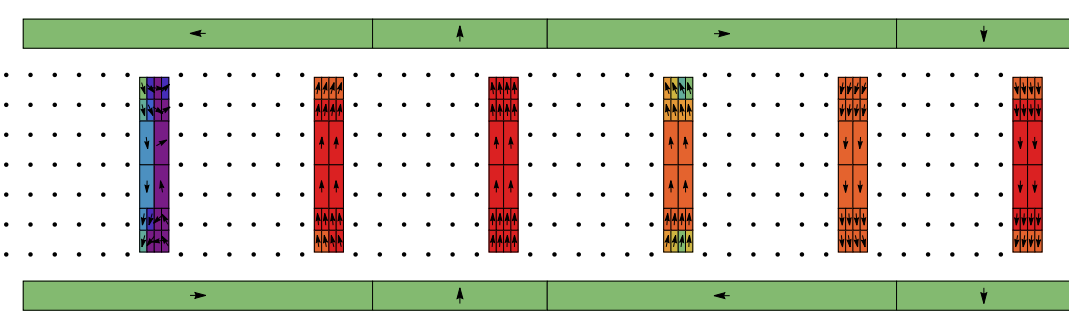
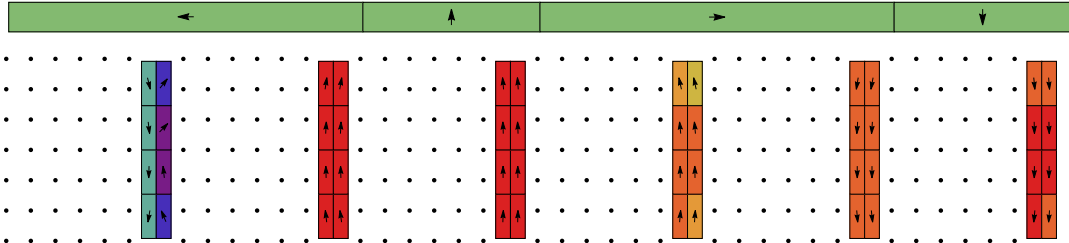


Figure 14: Illustrative PM magnetisations and analytic forces for a non-periodic segment of a PMLSM with soft iron slots. In (b-d), the coil filaments are shown with black dots and the slots are scaled to double the axial width for clarity. Each iron segment is the superposition of two PMs with radial and axial magnetisations. Dimensions and field equations are consistent with Figure 8 with the changes for $i = 1 \rightarrow 6$: filaments placed in circles $\frac{11}{24}$ mm in diameter and $z \rightarrow z_c \in [6i - 7, 6i - \frac{3}{2}]$ mm (an axial offset $z_o = -1$ mm); iron slots in $\rho \in [23.5, 29.5]$ mm, $z_s \in [6i - \frac{3}{2}, 6i - 1]$ mm; coil phase currents $\{\mathbf{A}, \mathbf{C}', \mathbf{B}, \mathbf{A}', \mathbf{C}, \mathbf{B}'\} = \frac{11}{3} \sin[(\pi/\tau)(\phi_z + z_o) + (i-1)\pi/3] \mathbf{A} \mathbf{e}_\varphi$ in $\varphi \in [0, 2\pi]$ rad with phase alignment $\phi_z = -\frac{13}{4}$ mm and pole pitch $\tau = 18$ mm.

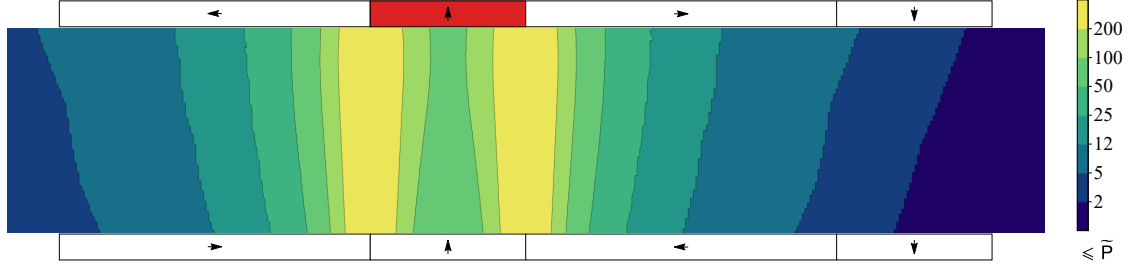


Figure 15: The adaptive number of terms required to guarantee a maximum remainder of $R = 10^{-2}$, using an efficient algorithm ([33, §A.D]), for the red-coloured radial PM field within the double-sided Halbach array of Figure 14. In a 3D analytic magnetic field solution there are eight terms due the geometry integration limits $\sum_{i,j,k=1}^2 (-1)^{i+j+k} f(\rho_i, \varphi_j, z_k)$, reducing to four in this axisymmetric 2D case with $\varphi \in [0, 2\pi]$. Thus, each sum contains a nested finite sum with a different number of terms; the average $\bar{P} = \frac{1}{4} \sum_{i,k=1}^2 P(\rho_i, z_k)$ is shown.

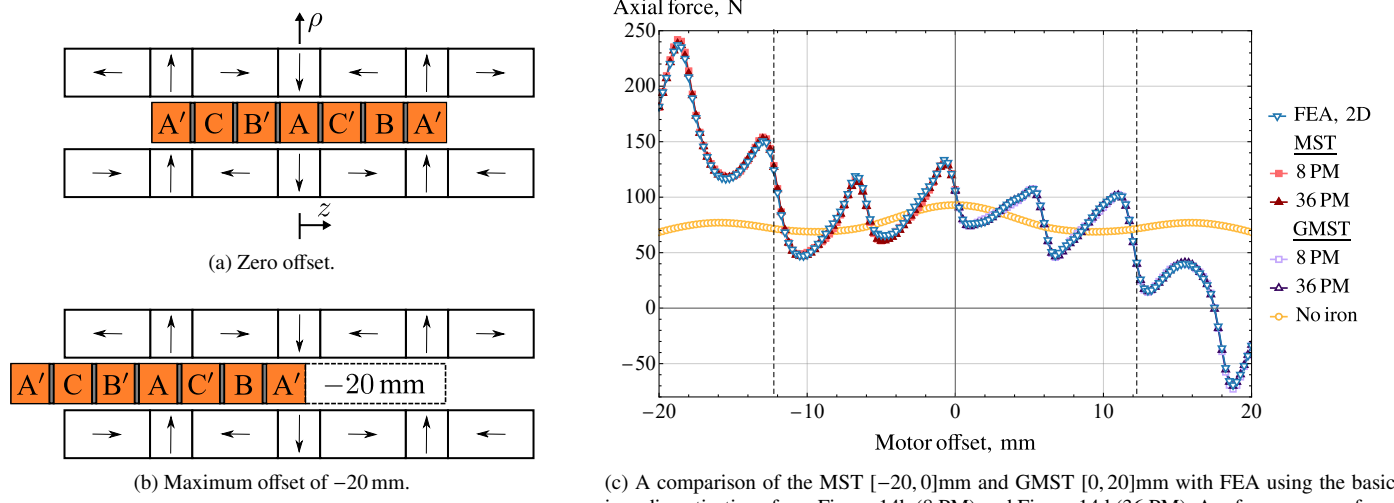


Figure 16: Magnetostatic forces on the slotted coil across a range of axial positions with positive (rightward) commutation. Regions with negative force would accelerate the coil in the opposite intended direction. The motor model is consistent with Figure 14, except for the addition of a coil and three Halbach PM segments. With this comes change in the coordinate origin: the coil array is shifted -20.75 mm and Halbach array -33 mm. The vertical dashed lines are where the coil array extrudes the Halbach array. Results are calculated with 500 mesh elements and $R = 10^{-2}\text{T}$, with the number of series terms in each summation P (Figure 15) capped at 100. Illustrations of the motor stroke are given in (b) and (c), that can be compared to Figure 8a.

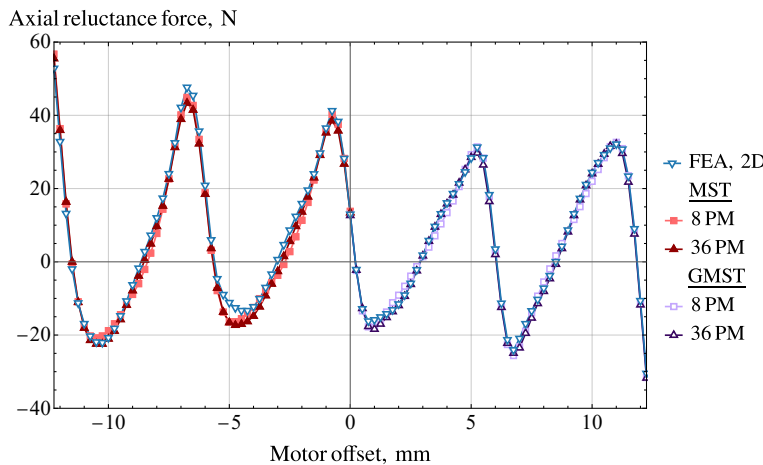


Table 1: Numeric results from Figure 16c ($[-20, 20]\text{mm}$) and Figure 17 ($[-12.5, 12.5]\text{mm}$): the Mean Average Error (MAE) and Mean Absolute Relative Error (MARE) compared to the FEA results.

	Figure 16c		Figure 17			
	Iron		Iron			
MST	8 PM	MAE (N)	MARE (%)	8 PM	MAE (N)	MARE (%)
	36 PM	1.9	7.6	2.0	2.2	2.8
GMST	8 PM	1.4	2.2	1.3	1.7	
	36 PM	0.9	2.8	0.9	1.3	

Figure 17: The reluctance force from Figure 16c, found by subtracting the ‘No iron’ result from the MST and GMST.

7. Conclusion

The Maxwell stress tensor (MST) is a function of a single arbitrary vector field, that is the superposition of the magnetic field from all sources in free space. Presented herein is a generalised Maxwell stress tensor (GMST), that is a function of two arbitrary vector fields: specifically, a distinction is made between the magnetic field from sources internal or external to a closed free space surface. The GMST is derived using a general divergence theorem identity, for which the MST is a special case of the GMST, with both implemented identically in computation. A thorough comparison is performed between the two stress tensors across three case studies that have analytic solutions, and three that only have semi-analytic or numeric solutions. Whilst the GMST is demonstrated in applications with two collections of magnetic objects, it can be readily applied to compute the force and torque between multiple arbitrary collections.

Error in the MST scales with the difference in magnitude between the external and internal fields. This is important for force calculation in actuators, as the magnetic field from coils is typically significantly lower than surrounding permanent magnets (PMs), and similarly with reluctance forces between PMs and iron. The MST is sensitive to inaccuracies in the field from a ‘coarse’ mesh, with errors quantified in the article using the volumetric divergence and curl through the closed region. Due to this, the MST is highly dependent on mesh topology and location; whereas the GMST requires less computational expense for an equivalent accuracy and is robust across differing meshes, including open surfaces. Application of both tensors, or boundary element methods, is limited by the availability and computational expense of magnetic field solutions. It is demonstrated that even if one has an analytic magnetic field solution, this does not always imply a useful solution.

The primary issue with the MST is sensitivity to magnetic field ‘inaccuracies’. Analytic magnetic field solutions are complex to derive, and are often expressed as an exact infinite series. For practical computation a finite sum is used, that will provide a solution accuracy proportional to the number of terms, and an offset in the force and torque result relative to the exact solution. With the culmination of all errors in the MST, a linear motor case study is presented in Section 6.2 where the MST (converged with a fine mesh and large number of series terms) has a >5 % mean absolute relative difference across the motor stroke to the GMST. The GMST is required for accuracy, robustness, and computational efficiency in parametric studies when implementing a model using superposition of elemental analytic magnetic field solutions.

CRediT authorship contribution statement

Matthew Forbes: Conceptualization, Formal analysis, Methodology, Software, Validation, Visualization, Writing – original draft. **William Robertson:** Conceptualization, Formal analysis, Funding acquisition, Methodology, Supervision, Visualization, Writing – review & editing. **Anthony Zander:** Conceptualization, Formal analysis, Supervision, Visualization, Writing – review & editing. **James Vidler:** Methodology, Software, Validation, Writing – review & editing. **Johannes Paulides:** Conceptualization, Funding acquisition, Supervision, Writing – review & editing.

Acknowledgements

The authors appreciate guidance from Prof. James Zanotti on the outset to finding an alternative Maxwell Stress Tensor form. This work was supported in part by the Advanced Electromagnetics Group; in part by the Australian Government Research Training Program Scholarship; and in part by the Faculty of SET, University of Adelaide.

References

- [1] Y.-C. Wu, B.-S. Jian, Magnetic field analysis of a coaxial magnetic gear mechanism by two-dimensional equivalent magnetic circuit network method and finite-element method, *Applied Mathematical Modelling* 39 (19) (2015) 5746–5758.
- [2] C. Birk, M. Reichel, J. Schröder, Magnetostatic simulations with consideration of exterior domains using the scaled boundary finite element method, *Computer Methods in Applied Mechanics and Engineering* 399 (2022) 115362.
- [3] B. Gysen, K. Meessen, J. Paulides, E. Lomonova, General formulation of the electromagnetic field distribution in machines and devices using Fourier analysis, *IEEE Transactions on Magnetics* 46 (1) (2010).
- [4] M.-F. Hsieh, Y.-C. Hsu, A generalized magnetic circuit modeling approach for design of surface permanent-magnet machines, *IEEE Transactions on Industrial Electronics* 59 (2) (2012) 779–792.
- [5] D. Krop, E. Lomonova, A. Vandeput, Application of Schwarz-Christoffel mapping to permanent-magnet linear motor analysis, *IEEE Transactions on Magnetics* 44 (3) (2008) 352–359.
- [6] J. Ruuskanen, A. Marteau, I. Niyonzima, A. Halbach, J. Vesa, G. Meunier, T. Tarhasaari, P. Rasilo, Multiharmonic multiscale modelling in 3-D nonlinear magnetoquasistatics: Composite material made of insulated particles, *Computer Methods in Applied Mechanics and Engineering* 425 (2024) 116945.
- [7] S. Lee, H. Kim, H. Son, Moment method based distributed multipoles for modeling magnetic materials in 2D and 3D magnetostatics, *Computer Methods in Applied Mechanics and Engineering* 393 (2022) 114692.
- [8] C. Custers, J. Jansen, M. van Beurden, E. Lomonova, 3D harmonic modeling of eddy currents in segmented conducting structures, *COMPEL* 38 (1) (2019) 2–23.
- [9] D. Trumper, W. Kim, M. Williams, Design and analysis framework for linear permanent-magnet machines, *IEEE Transactions on Industry Applications* 32 (2) (1996) 371–379.

- [10] J. Wang, G. Jewell, D. Howe, A general framework for the analysis and design of tubular linear permanent magnet machines, *IEEE Transactions on Magnetics* 35 (3) (1999) 1986–2000.
- [11] K. J. Meessen, J. J. H. Paulides, E. A. Lomonova, Force calculations in 3-D cylindrical structures using Fourier analysis and the Maxwell stress tensor, *IEEE Transactions on Magnetics* 49 (1) (2013) 536–545.
- [12] B. P. Ruddy, I. W. Hunter, A compact direct-drive linear synchronous motor with muscle-like performance, in: *IEEE International Conference on Robotics and Automation*, 2013, pp. 1498–1503.
- [13] R. Pile, J. Le Besnerais, G. Parent, E. Devillers, T. Henneron, Y. Le Menach, J.-P. Lecointe, Analytical study of air-gap surface force – application to electrical machines, *Open Physics* 18 (1) (2020) 658–673.
- [14] E. Furlani, Formulas for the force and torque of axial couplings, *IEEE Transactions on Magnetics* 29 (5) (1993) 2295–2301.
- [15] W. Robertson, B. Cazzolato, A. Zander, A simplified force equation for coaxial cylindrical magnets and thin coils, *IEEE Transactions on Magnetics* 47 (8) (2011) 2045–2049.
- [16] Z. Ren, Comparison of different force calculation methods in 3D finite element modelling, *IEEE Transactions on Magnetics* 30 (5) (1994) 3471–3474.
- [17] J. Li, K. T. E. Chua, H. Li, V.-T. Nguyen, D. J. Wise, G. X. Xu, C. W. Kang, W. H. R. Chan, On the consistency of three-dimensional magnetohydrodynamical lattice Boltzmann models, *Applied Mathematical Modelling* 132 (2024) 751–765.
- [18] T. Rabczuk, H. Ren, X. Zhuang, A nonlocal operator method for partial differential equations with application to electromagnetic waveguide problem, *Computers, Materials & Continua* 59 (1) (2019) 31–55.
- [19] W. Muller, Comparison of different methods of force calculation, *IEEE Transactions on Magnetics* 26 (2) (1990) 1058–1061.
- [20] F. Reich, W. Rickert, W. Müller, An investigation into electromagnetic force models: differences in global and local effects demonstrated by selected problems, *Continuum Mechanics and Thermodynamics* 30 (2) (2018) 233–266.
- [21] W. Rickert, W. H. Müller, Review of rational electrodynamics: Deformation and force models for polarizable and magnetizable matter, in: *Applications of Mathematics and Informatics in Natural Sciences and Engineering*, Vol. 334 of *Springer Proceedings in Mathematics & Statistics*, Springer International Publishing AG, Switzerland, 2020, pp. 245–280.
- [22] J. R. Melcher, *Continuum Electromechanics*, The M.I.T. Press, 1981.
- [23] C. Rinaldi, H. Brenner, Body versus surface forces in continuum mechanics: is the Maxwell stress tensor a physically objective Cauchy stress?, *Physical review. E, Statistical physics, plasmas, fluids, and related interdisciplinary topics* 65 (3 Pt 2B) (2002) 036615–036615.
- [24] A. Bossavit, Virtual power principle and Maxwell's tensor: which comes first?, *COMPEL* 30 (6) (2011) 1804–1814.
- [25] Z. Lee, Z. Xiao, Y. Tang, W. Zou, Analytical solutions of the magnetic and stress fields on a soft ferromagnetic material containing a smooth rigid inclusion in two-dimensional space, *Applied Mathematical Modelling* 118 (2023) 236–252.
- [26] M. Liu, K. Stierstadt, Electromagnetic force and the Maxwell stress tensor in condensed systems, *arXiv* (2000).
- [27] W. Deng, S. Zuo, Electromagnetic vibration and noise of the permanent-magnet synchronous motors for electric vehicles: An overview, *IEEE Transactions on Transportation Electrification* 5 (1) (2019) 59–70.
- [28] A. Bermudez, A. L. Rodriguez, I. Villar, Extended formulas to compute resultant and contact electromagnetic force and torque from Maxwell stress tensors, *IEEE Transactions on Magnetics* 53 (4) (2017) 1–9.
- [29] A. Bossavit, Bulk forces and interface forces in assemblies of magnetized pieces of matter, *IEEE Transactions on Magnetics* 52 (3) (2016) 1–4.
- [30] H. S. Choi, I. H. Park, S. H. Lee, Concept of virtual air gap and its applications for force calculation, *IEEE Transactions on Magnetics* 42 (4) (2006) 663–666.
- [31] J. L. O'Connell, W. S. Robertson, B. S. Cazzolato, Simplified equations for the magnetic field due to an arbitrarily-shaped polyhedral permanent magnet, *Journal of Magnetism and Magnetic Materials* 510 (2020) 166894.
- [32] R. Ravaud, G. Lemarquand, Magnetic field produced by a parallelepipedic magnet of various and uniform polarization, *Progress in Electromagnetics Research* 98 (2009) 207–219.
- [33] M. Forbes, W. S. P. Robertson, A. C. Zander, J. J. H. Paulides, The magnetic field from cylindrical arc coils and magnets: A compendium with new analytic solutions for radial magnetization and azimuthal current, *Advanced Physics Research* 3 (7) (2024) 2300136.
- [34] M. Forbes, W. S. P. Robertson, A. C. Zander, J. J. H. Paulides, Boundary-free analytic magnetic field calculations including soft iron and permanent magnets using an iterative discretization technique, *IEEE Transactions on Magnetics* 57 (2) (2021) 1–5.
- [35] E. P. Furlani, *Permanent Magnet and Electromechanical Devices: Materials, Analysis, and Applications*, Electromagnetism, Elsevier Science, 2001.
- [36] C. Truesdell, A form of green's transformation, *American Journal of Mathematics* 73 (1) (1951) 43–47.
- [37] C. Truesdell, R. Toupin, The classical field theories, in: *Principles of Classical Mechanics and Field Theory / Prinzipien der Klassischen Mechanik und Feldtheorie*, Springer Berlin Heidelberg, 1960, pp. 226–858.
- [38] W. Robertson, B. Cazzolato, A. Zander, Axial force between a thick coil and a cylindrical permanent magnet: Optimizing the geometry of an electromagnetic actuator, *IEEE Transactions on Magnetics* 48 (9) (2012) 2479–2487.
- [39] J. M. D. Coey, Hard magnetic materials: A perspective, *IEEE Transactions on Magnetics* 47 (12) (2011) 4671–4681.
- [40] K. J. Meessen, J. J. H. Paulides, E. A. Lomonova, Modeling and experimental verification of a tubular actuator for 20-g acceleration in a pick-and-place application, *IEEE Transactions on Industry Applications* 46 (5) (2010) 1891–1898.
- [41] M. Forbes, W. S. P. Robertson, <https://github.com/AUMAG/mag-cyl-field> (2024).
- [42] J. A. Stratton, *Electromagnetic theory*, 1st Edition, International series in physics, McGraw-Hill, New York, 1941.
- [43] M. Forbes, W. S. P. Robertson, <https://github.com/AUMAG/mag-gmst-force> (2025).

Appendix A. Finding an equivalent set of permanent magnet magnetisations for soft iron

The relative permeability

$$\mu_r(\mathbf{r}) = \frac{\mathbf{B}(\mathbf{r})}{\mu_0 \mathbf{H}(\mathbf{r})} \quad (\text{A.1})$$

is unity in a vacuum, or through a material that has invariant properties in an external magnetic field. When the relative permeability is a function of magnetic field strength, position, and/or direction, then respectively, the material is nonlinear, inhomogeneous, and/or anisotropic. In these cases the constitutive relation is

$$\mathbf{M}(\mathbf{r}) = [\mu_r(\mathbf{r}) - 1]\mathbf{H}(\mathbf{r}). \quad (\text{A.2})$$

The analytic magnetic field models in this article are achieved by assuming linear and homogeneous matter. This requires the assumption that both the magnetic flux density and magnetic field strength are uniform through a region of matter. In the case

of soft iron, this is achieved through discretisation and superposition, with each segment containing a principal magnetisation of $\mathbf{M} = M_\perp(\cos\varphi^*\mathbf{e}_x + \sin\varphi^*\mathbf{e}_y) + M_\rho\mathbf{e}_\rho + M_\varphi\mathbf{e}_\varphi + M_z\mathbf{e}_z$. The material properties are isotropic, but the effect of physical properties such as laminations can be modelled by weighting or removing basis vectors, e.g. $H_z = M_z = 0$.

The relative permeability in this article is from a soft magnetic composite, that is fit using the conditional relation:

$$\check{B}(H) = \begin{cases} (3.64 \times 10^{-4} - \mu_0)H, & H < 55, \\ \frac{0.9429\tilde{H}_1^2 + 2.284\tilde{H}_1 + 1.396}{\tilde{H}_1^2 + 2.181\tilde{H}_1 + 5.826}, & 55 \leq H < 630, \\ \frac{2.358\tilde{H}_2^2 + 5.043\tilde{H}_2 + 2.307}{\tilde{H}_2^2 + 2.62\tilde{H}_2 + 1.327}, & 630 \leq H < 10^5, \\ 1.624 \times 10^{-6}H + 1.975, & 10^5 \leq H < 3.05 \times 10^5, \\ \mu_0 H + 2.087, & 3.05 \times 10^5 \leq H. \end{cases} \quad (\text{A.3})$$

where $\tilde{H}_1 = (H - 240.3)/201.9$ and $\tilde{H}_2 = (H - 1.71 \times 10^4)/2.556 \times 10^4$ [34], plot in Figure A.1. The conditional analytic expression of (A.3) can be freely replaced with another expression, or even an interpolated lookup table, such as that required for use in FEA software. An algorithm to solve for the iron magnetisations, or equivalent PM magnetisations, is given in Algorithm 1. This requires the magnetic field strength of each iron segment to be found using the magnetic flux density $\check{B}(B)$. In this article a tolerance (tol) of 1000 A/m or ≈ 1.3 mT is used for all results. The algorithm has two simple computational improvements: not calculating the field from iron segments on centroids that are significantly far away; not re-calculating the field from an iron segment if there was no significant change in magnetisation (convergence requires all magnetisations to have not changed within tol).

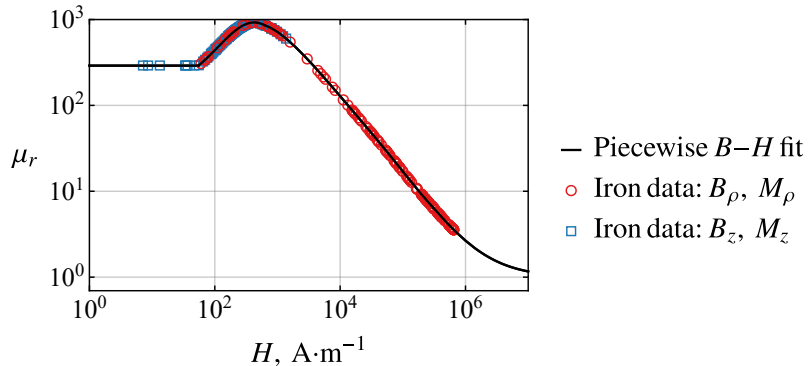


Figure A.1: The relative permeability (A.2) of the material defined by (A.3). Overlaid is relative permeability data from the computation of Figure 14d, split into axial and radial components.

Table A.1: New variable definitions for Algorithm 1.

Variable	Definition
\mathbf{r}_c	Iron segment centroids
$\mathbf{B}_0(\mathbf{r}_c)$	$\mathbf{r}_c = r_{cp}\mathbf{e}_\rho + r_{cz}\mathbf{e}_z$
$\mathbf{B}_l(\mathbf{r}_c)$	Magnetic field from all non-iron sources
\mathbf{B}_l	Current iteration magnetic field from all iron sources
$\ \mathbf{M}(\mathbf{r}_c)\ $	$\mathbf{B}_l = B_{lp}\mathbf{e}_\rho + B_{lz}\mathbf{e}_z$
$\ \mathbf{M}(\mathbf{r}_c)\ _{\text{prev}}$	Current iteration magnetisation magnitude
i, j	$\mathbf{M} = M_\rho\mathbf{e}_\rho + M_z\mathbf{e}_z$
tol	Previous iteration magnetisation magnitude
	Index for equal size lists: $\mathbf{B}_0, \mathbf{B}_l, \mathbf{M}, \mathbf{r}_c, \rho', z'$.
	Iteration stop condition in A/m

Algorithm 1 Iterative procedure to find the magnetisation of each iron segment in 2D cylindrical coordinates using the B - H curve (A.3), with definitions given in Table A.1.

```

1: function IRONITERATION2D( $\mathbf{B}_0$ ,  $\mathbf{r}_c$ ,  $\rho'$ ,  $z'$ )
2:    $\mathbf{B}_I = 0$                                  $\triangleright$  Initial iron  $\mu_r = 1$ 
3:    $\|\mathbf{M}\| = 0$ 
4:    $\|\mathbf{M}\|_{\text{Prev}} = \|\mathbf{M}\|$             $\triangleright$  Check condition after first execution
5:   while  $|\|\mathbf{M}\| - \|\mathbf{M}\|_{\text{Prev}}| > \text{tol}, \forall \mathbf{M}$  do
6:      $\|\mathbf{M}\|_{\text{Prev}} = \|\mathbf{M}\|$ 
7:     for  $i$  in  $\mathbf{B}_0$  do                   $\triangleright$  Magnetisation calcs.
8:        $\|\mathbf{B}\| = \|\mathbf{B}_0^{(i)} + \mathbf{B}_I^{(i)}\|$        $\triangleright \ell^2$  norm
9:        $\hat{\mathbf{B}} = \frac{\mathbf{B}_0^{(i)} + \mathbf{B}_I^{(i)}}{\|\mathbf{B}\|}$            $\triangleright$  Normalise components
10:       $H = \check{H}(\|\mathbf{B}\|)$                  $\triangleright$  Interpolate or solve for H
11:       $\|\mathbf{M}\|^{(i)} = \frac{\check{B}(H)}{\mu_0} - H$          $\triangleright$  Or use  $\|\mathbf{B}\|$ 
12:       $M_\rho^{(i)} = \hat{B}_\rho \|\mathbf{M}\|^{(i)}$            $\triangleright$  Radial PM
13:       $M_z^{(i)} = \hat{B}_z \|\mathbf{M}\|^{(i)}$            $\triangleright$  Axial PM
14:      for  $j$  in  $\mathbf{r}_c$  do                   $\triangleright$  Field calcs. [41]
15:         $B_{l\rho}^{(i,j)} = \text{BpAna}(M_\rho^{(i)}, \mathbf{r}_c^{(j)}, \rho'^{(i)}, z'^{(i)})$ 
16:         $B_{lz}^{(i,j)} = \text{BzAna}(M_z^{(i)}, \mathbf{r}_c^{(j)}, \rho'^{(i)}, z'^{(i)})$ 
17:      end for
18:    end for
19:     $\mathbf{B}_I = \sum_i (B_{l\rho}^{(i,j)} \mathbf{e}_\rho + B_{lz}^{(i,j)} \mathbf{e}_z)$ 
20:  end while
21:  return  $\mathbf{M} = M_\rho \mathbf{e}_\rho + M_z \mathbf{e}_z$            $\triangleright \forall \mathbf{r}_c$ 
22: end function

```

Appendix B. Application of the divergence theorem given singularities in the GMST region

Continuing the discussion of Section 3, to apply the divergence theorem linking \mathbf{B} through \mathcal{V}_1 to \mathbf{B} on $\partial\mathcal{V}_1$, a continuously differentiable \mathbf{B} is required throughout \mathcal{V}_1 . From (2), it can be seen that each i , j , and k sub-region within \mathcal{V}_1 will create a multiply-connected region of singularities. We define each singular region that is to be removed: $\sum_m^l \partial\mathcal{V}_2^{(m)}$, where $l = i + j + k$, that is subtracted from (13) to give

$$\mathbf{F} = \oint_{\partial\mathcal{V}_1} \mathcal{F}(\mathbf{B}_E, \mathbf{B}_I) \cdot d\mathbf{s} - \sum_m^l \lim_{a^{(m)} \rightarrow 0} \oint_{\partial\mathcal{V}_2^{(m)}} \mathcal{F}(\mathbf{B}_E^{(m)}, \mathbf{B}_I^{(m)}) \cdot d\mathbf{s}. \quad (\text{B.1})$$

Knowledge of the location of each surface containing a singularity is seemingly required, along with the internal magnetic field. These singularities can be divided into infinitesimal volumes containing single magnetic dipoles (current model \mathbf{m}_J and/or charge \mathbf{m}_ϱ model, $\text{A}\cdot\text{m}^2$), that locally have a uniform external field. The limit of the force on the volume is when it shrinks to a point with an undefined internal field, found from integrating (1)

$$\begin{aligned} \mathbf{F} &= \nabla \int_V \mathbf{M}_J dv \cdot \mathbf{B}_E - \mathbf{B}_E \cdot \nabla \left(\int_V \mathbf{M}_J dv \right) + \int_V \mathbf{M}_J dv \cdot (\nabla \mathbf{B}_E) + (\nabla \mathbf{B}_E) \cdot \int_V \mathbf{M}_\varrho dv, \\ &= \nabla \mathbf{m}_J \cdot \mathbf{B}_E - \mathbf{B}_E \cdot \nabla \mathbf{m}_J + \mathbf{m}_J \cdot (\nabla \mathbf{B}_E) + (\nabla \mathbf{B}_E) \cdot \mathbf{m}_\varrho, \end{aligned} \quad (\text{B.2})$$

with the magnetic shell model [42, pg.237] $\mathbf{J} \equiv \nabla \times \mathbf{M}_J$, and vector identity $(\nabla \times \mathbf{c}) \times \mathbf{b} = (\nabla \mathbf{c}) \cdot \mathbf{b} - \mathbf{b} \cdot (\nabla \mathbf{c})$. As each surface $\partial\mathcal{V}_2^{(m)}$ encloses upon the singularity with some fictitious radii $a^{(m)} \rightarrow 0$, illustrated in Figure B.1, there is no net average force in the immediate surrounding region

$$\sum_m^l \lim_{a^{(m)} \rightarrow 0} \oint_{\partial\mathcal{V}_2^{(m)}} \mathcal{F}(\mathbf{B}_E^{(m)}, \mathbf{B}_I^{(m)}) \cdot d\mathbf{s} \equiv \mathbf{0}. \quad (\text{B.3})$$

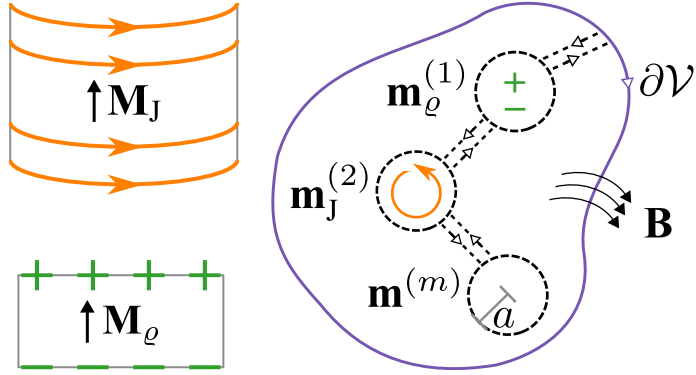


Figure B.1: Illustration of a simply connected region with infinitesimal magnetic dipole \mathbf{m} singularities at $1/r^{(m)}$, from magnetised \mathbf{M} regions, and surrounded with spheres of radii a . The field \mathbf{B} through the region $\partial\mathcal{V}$ is continuous apart from jump discontinuities in the spheres, where the magnetisation or current abruptly goes to zero, without a smooth transition layer.

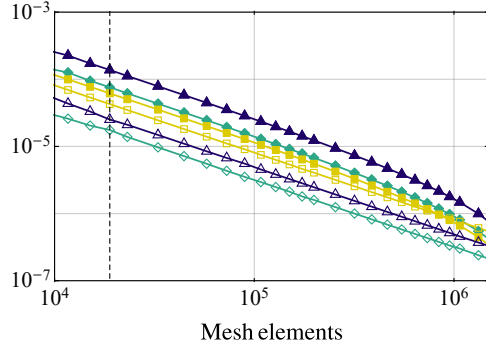
This implies the location of the singularities are arbitrary, given the region $\partial\mathcal{V}_1$ is significantly far from the singularities. We can re-write (B.1) with (B.3) to give a simply connected region that is continuously differentiable

$$\mathbf{F} = \oint_{\partial\mathcal{V}} \mathcal{F}(\mathbf{B}_E, \mathbf{B}_I) \cdot d\mathbf{s}, \quad (\text{B.4})$$

where $\partial\mathcal{V} = \partial\mathcal{V}_1 - \partial\mathcal{V}_2$.

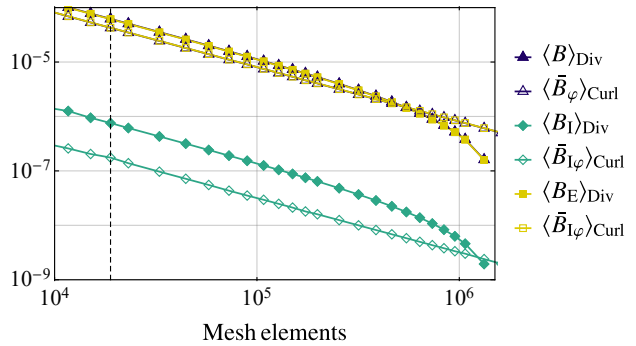
Appendix C. Additional figure detail

Average field error, T



(a) 3D mesh convergence, where $\mathbf{M}_I = -\mathbf{M}'_E$.

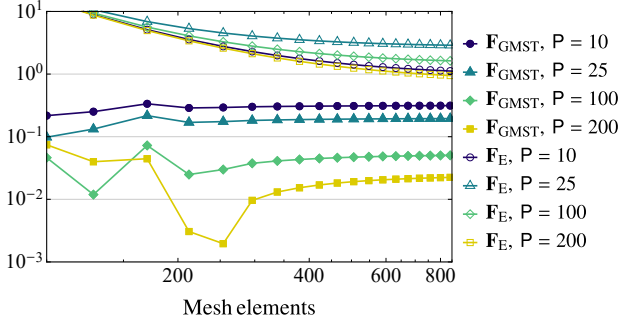
Average field error, T



(b) 3D mesh convergence, where $\mathbf{M}_I = -\frac{1}{100}\mathbf{M}'_E$.

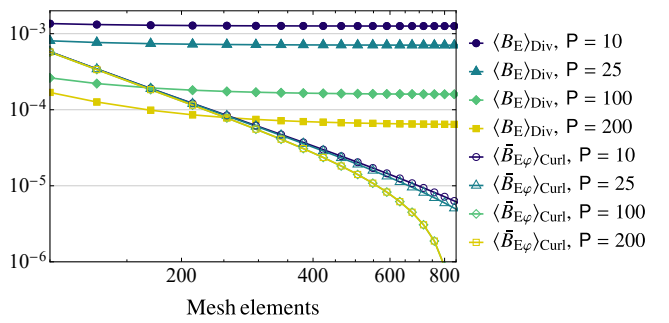
Figure C.1: Zoomed-in version of Figure 5.

Axial force, $|\tilde{F}|_{\text{Analytic}} \%$



(a) Force error.

Average field error, T



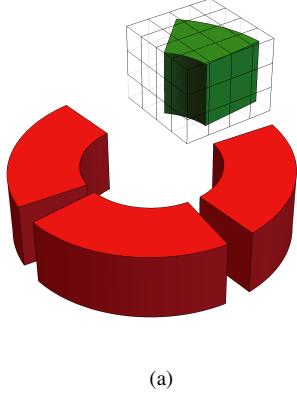
(b) Magnetic field error.

Figure C.2: Zoomed-in version of Figure 9.

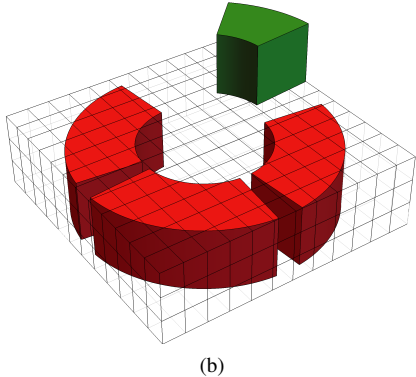
Appendix D. Supplementary material: 3D force and torque

The case studies in this article are reproducible using the supplemental material and online repository [43]. For simplicity in representing results, the practical case studies in this article are limited to axial forces and torques; however, the tensors are used to return all orthogonal components of force and torque. Additionally, it was not demonstrated in the article that meshing either collection of magnetic sources will generate an equivalent result, albeit equal and opposite. A simple case study is summarised in this section, generated from a Mathematica notebook in the supplementary material and using an accompanying Mathematica package that contains all analytic magnetic field solutions cited in this article.

A constant mesh density is maintained for each equivalent refinement in Table D.1 and Table D.2, with the latter covering $4.7 \times$ the area. This increase in area leads to a higher computation expense, but results can be seen to converge to equal magnitudes and agree with that of the FEA model. The FEA model was run until convergence was met for both force and torque magnitudes, to the displayed significant figures.



(a)



(b)

Table D.1: Results from Figure D.1a.

Model	Mesh elements	\mathbf{F} , N			\mathbf{T} , mN·m		
		F_x	F_y	F_z	T_x	T_y	T_z
GMST	64	0.421	0.173	1.047	-1.062	-0.784	1.695
	288	0.376	0.126	1.019	-0.719	-0.993	1.319
	1008	0.373	0.123	1.014	-0.699	-0.995	1.290
	4560	0.372	0.123	1.013	-0.698	-1.000	1.288
	18480	0.371	0.122	1.013	-0.697	-1.001	1.287
FEA	-	0.371	0.123	1.013	-0.698	-1.002	1.287

Table D.2: Results from Figure D.1b.

Model	Mesh elements	\mathbf{F} , N			\mathbf{T} , mN·m		
		F_x	F_y	F_z	T_x	T_y	T_z
GMST	280	-0.365	-0.098	-1.034	0.530	1.198	-1.159
	1200	-0.372	-0.125	-1.014	0.711	1.001	-1.310
	5376	-0.371	-0.122	-1.013	0.696	1.002	-1.286
	21840	-0.371	-0.122	-1.013	0.697	1.002	-1.286
	88032	-0.371	-0.122	-1.013	0.697	1.001	-1.286
FEA	-	-0.371	-0.123	-1.013	0.698	1.002	-1.287

Figure D.1: Equivalent calculations for the force and torque magnitude between diametrically magnetised permanent magnets, using (34) with field equations \mathbf{B}_E and \mathbf{B}_I from [33, §5.1]. For Table D.1, illustrated in (a), the single PM has magnetisation $|\mathbf{M}_{\perp}| = 800 \text{ kA/m}$ at angle $\varphi^* = \frac{\pi}{4}$ with geometry $\rho \in [5, 10] \text{ mm}$, $\varphi \in [\frac{\pi}{32}, \frac{\pi}{4}]$, $z \in [6, 11] \text{ mm}$. The remaining PMs have magnetisations $|\mathbf{M}'_{\perp}| = 955 \text{ kA/m}$ at angles $\varphi^{*(i)} = i\frac{\pi}{4}$ with geometries $\varphi^{(i)}$, z' given in Figure 13, with changes $\rho' \in [5, 10] \text{ mm}$, $\theta = \frac{\pi}{32}$, $N = 4$ and $i = 2 \rightarrow 4$. For Table D.1, illustrated in (b), the primed and unprimed coordinates are reversed, or the internal and external field definitions are reversed.